VORLAX2024: Further Upgrades to a Legacy Potential Flow Solver

Timothy T. Takahashi[1], Jack A. Griffin,[2] Brandon S. Gaydusek[3], *and* William P. Lorenzo[2]
Arizona State University, Tempe, AZ, 85287-6106

VORLAX **is a generalized subsonic/supersonic vortex-lattice potential flow solver written by Luis R. Miranda for Lockheed California in the early 1970's. This paper describes further methods to improve code functionality and solution quality which arose from discoveries made while benchmarking its application to slender aircraft configurations at extremely high flight speeds. While the fundamental supersonic Vortex lattice formulation used in** ***VORLAX*** **was correct, congenital problems in the original solution processor somewhat degraded the quality of its results. The revised code, which embodies several subtle changes, no longer violates experimentally determined pressure limits and better matches classic high-speed aircraft wind-tunnel results, specifically when run at sideslip. In this new paper, we benchmark** ***VORLAX*** **against a large number of NACA and early NASA era wind tunnel tests and document the improvement these code revisions make on the quality of its results.**

Nomenclature

α = Angle of Attack (deg)
C_D = Drag Coefficient
C_L = Lift Coefficient
Cp = Pressure Coefficient
M = Mach Number
NVOR = Spanwise Control Points
RNCV = Chordwise Control Points
t/c = Thickness Normalized to Chord

I. Introduction

COMPUTATIONAL AERODYNAMICS has revolutionized engineering approaches to aircraft design. While modern, volume-grid CFD methods have become entrenched in aircraft detail design, there remains a need for fast and accurate panel methods. [1] Fundamentally, nothing has changed in the last 40 years that renders panels methods obsolete. In 2020, my student T.J. Souders and I embarked on a quest to modernize the evergreen vortex-lattice code, *VORLAX*; producing *VORLAX2020*.[2][3][4][5] This paper describes the technical basis for further changes to the code arising from an extensive effort to benchmark supersonic aircraft aerodynamic design problems, *VORLAX2024d*. The revisions address latent issues found in the original 1977 version which address solutions at high sideslip angles and solutions at very high Mach numbers. [2]

---

[1] Professor of Practice (retired), School for Engineering of Matter, Transport & Energy, P.O. Box 876106, Tempe, AZ. Associate Fellow AIAA

[2] M.S. Graduate, Aerospace Engineering, P.O. Box 876106, Tempe, AZ. Student Member AIAA.

[3] M.S. Candidate, Aerospace Engineering, P.O. Box 876106, Tempe, AZ. Student Member AIAA.

II.What is VORLAX ?

A. General Usage and Capabilities

VORLAX is a potential flow solver utilizing a generalized vortex lattice method to resolve flow field behavior for shock-free, attached-flow conditions [2]. *VORLAX* is unique among widely available solvers (for example, *AVL* [6], *Tornado* [7] and *VSPAero* [8]) in that it has an ability to solve flows at subsonic, transonic, and supersonic freestream Mach numbers. While the code cannot expressly capture a shockwave, it automatically switches between subsonic and supersonic flow influence coefficients. The supersonic flow model captures many of the characteristics associated with supersonic leading-edge flows.

One reason that *VORLAX* remains such a powerful and useful stem from its simple “flat-file” input deck, a legacy of its origins as a FORTRAN IV code. *VORLAX2024d* reliably compiles on Intel Visual Fortran so long as select legacy syntax flags are enabled.

VORLAX reads input files which define flight configuration information and geometric properties of the body in a simple 10-column format, allowing rapid preprocessing of hundreds of test cases using a simple scripting language capable of writing text files, such as *MATLAB*, *VBA*, or Python.

FIGURE 1 depicts an airliner wing/body configuration with its standard coordinate system. *VORLAX* geometry is compatible with standard aircraft lofting practice. The *x*-axis represents the frame station and grows more positive as one moves aft. The *z*-axis represents the water line and grows more positive as one moves up. The *y*-axis is aligned to form a traditional, right-handed coordinate system.

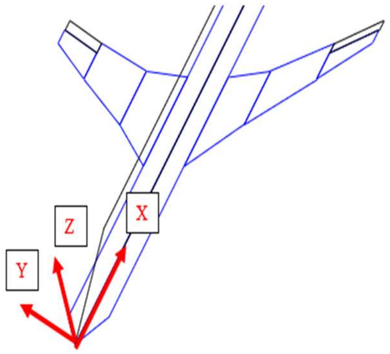

FIGURE 1 - *VORLAX* Panel Method Representation of an Aircraft.

B. How *VORLAX* handles Mach effects, sweep and thickness

VORLAX estimates the velocity fields over a complex geometry through a linear superposition of’ fields induced by simple vortex geometries.[2] Compressibility effects are governed by terms involving, $\beta = \sqrt{1 - {M_\infty}^2}$ or $\sqrt{{M_\infty}^2 - 1}$; where M_∞ is the freestream Mach number. To permit the solution of arbitrary geometries, Miranda implemented a swept horse-shoe vortex formation – where the vortex is “defined by the addition of the corresponding fields induced by three rectilinear segments: a transverse skewed segment, and two trailing legs. Following Ward [9] Miranda formulates a single expression to represent the vortex influence based on whether the global flow is subsonic ($\beta^2>0$) or supersonic ($\beta^2<0$). These schemes also allow the flat plate solutions to easily be extended to simulate thickness and volume effects. Thus, *VORLAX* may compute net pressures across a thin panel or surface pressure distributions over “sandwich panels” using a common vortex-lattice basis.

VORLAX computes sideslip effects using a hybrid method, designed to obtain “reasonably accurate sideslip effects using only a first order perturbation solution but without all of the geometrical complications inherent in the skewed—wing approach” [2] As noted above, *VORLAX* develops a vortex lattice representation of the configuration and its associated vortex wake through bound and free elements. For *VORLAX*, the bound portion of the lattice, containing both transverse and trailing, or chordwise, segments, is held in an invariant body axis form, where the chordwise legs are parallel to the lofting *x*-axis; see FIGURE 2.

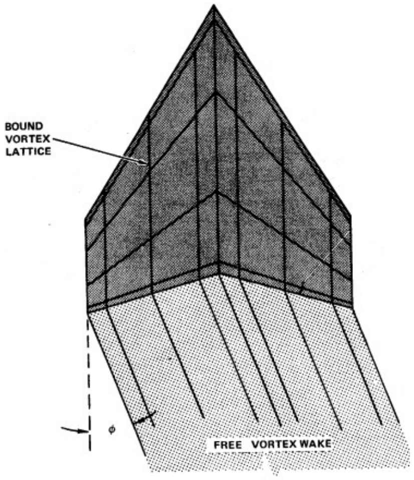

FIGURE 2 - *VORLAX* Representation of Sideslip. [2]

VORLAX also augments rolling moments of each element with an estimate of the local rolling couple due to the sideslip angle; this term is internally referred to as *SICPLE*.

C. Basic Grid Structure

The most basic geometric representation in *VORLAX* is the "flat panel" mode. This works by representing the geometry in terms of a collection of trapezoids, where the defining chord sections may be of uneven length and *x*-axis starting position but also must be parallel to the *x*-axis. The code further discretizes this trapezoid into sub-elements as defined by a spanwise number of control points (*NVOR*) and a chordwise number of control points (*RNCV*); see FIGURE 3.

Continuing from the discussion regarding cambered panels, it is possible to simulate wing thickness effects, including conventional, diamond or wedge-shaped airfoils by arranging a pair of single-impermeable panels with a small amount of separation between one another. FIGURE 4 shows the "venetian blind" representation of a wedge airfoil by a pair of thin cambered panels – where each element has a local inclination relative to the panel surface. Through the *ITS* flag, *VORLAX* may apply the zero-mass flux condition to either both, the inner or the outer "wetted" surface.

D. Axis Systems

The original version of *VORLAX* as presented in Miranda's original NASA Contractor Report presents lift, drag, side force, pitching moment, rolling moment, and yawing moment in Wind Axis. Compared to a bod*y*-fixed coordinate frame, the wind axis is fully rotated in both angle-of-attack and sideslip angle. The original code develops these forces and moments in terms of the "lofting" sign convention where +*X* extends aft, +*Y* extends out a forward-facing pilot's right ear and +*Z* is up, whereas aircraft customary axes have +*X* extending forward out the nose, +*Y* out the forward-facing pilot's right ear and +*Z* pointing down. Thus, the internal computations invert the sign of the rolling and yawing moment compared to current practice.

Later versions of *VORLAX* supported by Takahashi adjusted the signs of rolling and yawing moments to provide a more standard basis for aerodynamic data. *VORLAX2020* and prior compiles present tabular data in terms of Aircraft Customary Stability Axis. [3][4][5] *VORLAX2024d* presents tabular data in both modern Aircraft Customary Stability Axis and Aircraft Customary Body Axis.

Modern aerodynamics engineers utilize "Stability Axis;" see FIGURE 5. [10] The USAF describes the stability axis system as one where the *x*-axis aligns itself with the wind from a pitch plane perspective and with the body from a yaw plane perspective. The *z*-axis represents vertical heights, where *z* grows more positive as

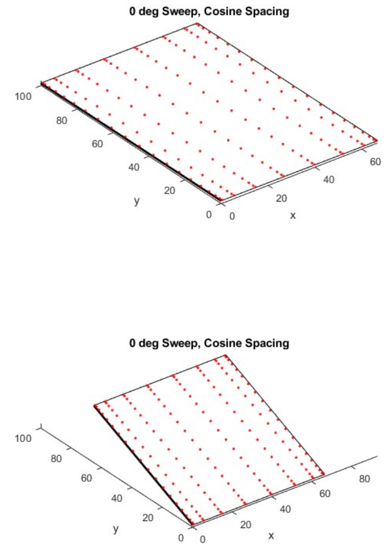

FIGURE 3 - Flat Panel Visualization with Grid Points.

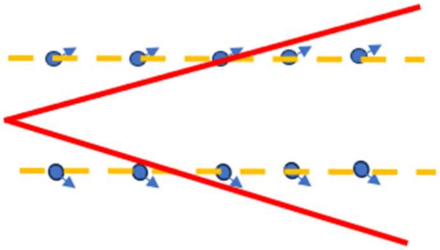

FIGURE 4 - *VORLAX* Thickness representation of a wedge airfoil.

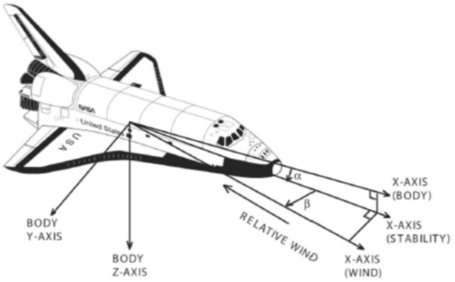

FIGURE 5 - Comparison of Wind, Body, and Stability Axis.

one moves down. The *y*-axis is aligned to form a traditional, right-handed coordinate system; the *y*-axis in modern stability axis is precisely aligned with the bod*y*-axis *y*-axis. Similarly, the body-axis right-hand-rule reference frame has the *x*-axis aligned with the aircraft's centerline; movement towards the nose leads to a positive change in the *x* coordinate. The *z*-axis represents the water line, but opposite to the lofting reference frame, it grows more positive as one moves down. The *y*-axis is aligned to form a traditional, right-handed coordinate system; a positive torque about the *y*-axis is a nose-up pitching moment.

Modern GN&C engineers prefer to work in a bod*y*-fixed reference frame; see FIGURE 5. In this right-hand-rule reference frame, the *x*-axis is aligned with the longitudinal axis of the fuselage with movement towards the nose leading to a positive change in the x coordinate. The *z*-axis represents the water line, but opposite to the lofting reference frame, it grows more positive as one moves down. The *y*-axis is aligned to form a traditional, right-handed coordinate system; a positive torque about the *y*-axis is a nose-up pitching moment. The revised *VORLAX2024d* first integrates surface pressures into body axis forces and moments; then performs any necessary transformations.

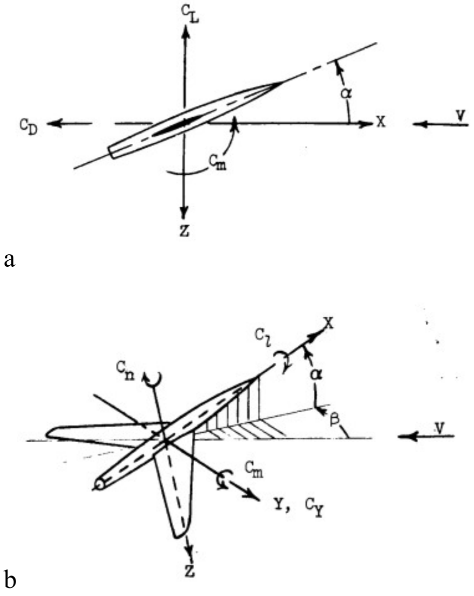

FIGURE 6 - Older hybrid axis system. Example from NASA TM-*X*-287. [11]

In our extensive benchmark studies of early supersonic configurations, we recognize that older NACA and NASA papers may utilize an alternative hybrid coordinate system where Lift, Drag and Pitching moments are given in a wind aligned reference frame while side-force, rolling moments and yawing moments are given in a body aligned reference frame; see FIGURE 6. [11] This is subtly different from modern stability axis; discrepancies grow as the sideslip angle, β, increases.

III. Discovery and Remedy of Long-Standing "Bugs"

Since Souders & Takahashi's 2020 update, *VORLAX* maintains a few known issues arising from its conceptualization back in the 1970's. [2] Some of these issues are endemic to panel methods, others have been resolved in the 2024 edition.

One unresolvable issue is that the method to integrate the induced drag C_{D_i} falls apart when using the "linear" chordwise spacing grid mode. While this is easily remedied by utilizing the alternative "cosine" grid spacing, it makes verification and validation of the results more difficult due to the inability to maintain equidistant grid spacing during grid refinement studies. This is a result of *VORLAX* utilizing Lan's Method to compute the leading-edge thrust coefficient. [9] Our input processor will terminate any models which utilize the analytical leading-edge suction correction concurrently with a linear chordwise grid (as controlled by the *LAX* flag).

A second unresolvable issue is that the method to integrate the induced drag C_{D_i} proves unreliable when using sandwich panels. This is because a "sandwich panel" model inherently captures only a fraction of the total leading-edge suction as a result of its coarse paneling while the thin-panel analytical correction would double-count effects.

Calibration runs comparing *VORLAX* models of classic high-speed aircraft, like the Bell X-1, Bell X-2 and North American X-15 revealed several other issues. These include: 1) potential solution instabilities when complex geometries are modelled near the speed of sound, 2) solution instabilities for complex geometries modelled at "critical" supersonic speeds, 3) non-physical surface pressures for supersonic "sandwich panel" models, 4) dihedral-effect inconsistencies due to the order of operations during surface pressure integrations, and 5) minor inconsistencies in the stability axis transformation equations. These deficiencies have been addressed in the 2024 code update.

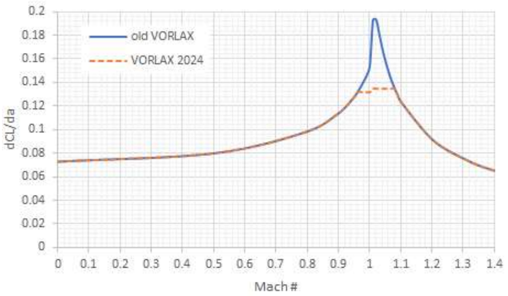

FIGURE 7 - Lift Curve Slope (*dCL/dα*) for an AR=6, thin wing as a function of freestream Mach number. "Ur *VORLAX*" vs. *VORLAX2024*.

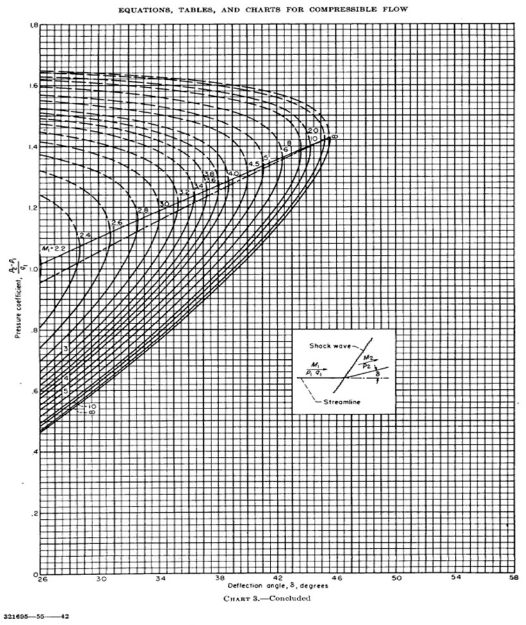

FIGURE 8 – Maximum pressure coefficient developed in supersonic flow with a "strong" i.e., attached shock wave. After NACA 1135. [13]

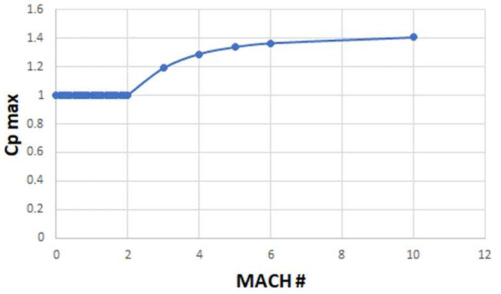

FIGURE 9 – *Cpmax* as a Function of Mach # - digitized from NACA 1135. [13]

A. Improving Solution Robustness at Near Sonic Speeds

To improve the robustness of solutions at near sonic speeds, *VORLAX2024d* limits the value of $\beta^2 = 1 - {M_\infty}^2$ from approaching zero. To ensure relative continuity of the lift slopes, β^2 is limited to be no greater than -0.078 for subsonic flow conditions (i.e., limiting the Prandtl-Glauert effect to freestream speeds no faster than Mach 0.96) and no less than +0.166 for supersonic flow conditions (i.e., limited the Ackert effect to freestream speeds no slower than Mach 1.08). This "softens" the theoretical lift-slope rise at sonic speeds to about double the incompressible value. FIGURE 7 demonstrates the effects of this change when analyzing a thin Aspect Ratio 6 wing. This improves solution robustness, especially for dense models with skewed grid cells.

B. Non-Physical Surface Pressures for Thin Panel Models

After *VORLAX* computes the necessary vortex strengths to impose no-flow conditions about its panels, it computes the differential pressure at each node point. Older versions of *VORLAX* did not limit net pressures; this has been revised in *VORLAX2024d*.

The low-pressure limit of airflow is the pressure coefficient which corresponds to a pure vacuum:

$$Cp_{vac} = \max\left(-142.86\,, \frac{-1.4286}{M^2} \right)$$

Prior studies [12] found that physical flows can rarely achieve *Cp*'s much lower than a 70% vacuum. Therefore, for *VORLAX2024d*, we will revise the Cp_{min} limit to:

$$Cp_{min} = 0.7\ Cp_{vac}$$

Thus, for a thin panel, the maximum net pressure, $\overline{Cp_{net}}$, must not exceed the difference between *Cpmin* (70% vacuum) and *Cpmax* .

What, then, is an appropriate estimate of *Cpmax* for a thin, inclined flat plate? Only under the pure incompressible (i.e., *M*=0) assumption does stagnation pressure equal the sum of the static pressure and the dynamic pressure. At higher speeds, the maximum static pressure developed by a thin panel model will have a limiting pressure governed by the maximum turning angle, see FIGURE 8 from NACA 1135. [13] We may thus digitize and plot this data as FIGURE 9.

Taking these two trends together, we may build a function to limit the maximum net pressure differential across a thin, inclined flat plate; see FIGURE 10. At incompressible speeds, $Cp_{min} = -100$ while $Cp_{max} = +1$; therefore $-101 < Cp_{net} < +101$. At Mach 1, $Cp_{min} = -1.001$ while $Cp_{max} = +1$; therefore $-2.001 < Cp_{net} < +2.001$. At Mach 5, $Cp_{min} = -0.04$ while $Cp_{max} = +1.337$; therefore $-1.377 < Cp_{net} < +1.377$.

C. Non-Physical Surface Pressures for Sandwich Panel Models

Similarly, for Sandwich Panel models, after *VORLAX* computes the necessary vortex strengths to impose no-flow conditions about its panels, it computes the actual surface pressure at each node point. Since its inception, *VORLAX* has limited both positive and negative pressures; however, extensive benchmarking of supersonic aircraft revealed a fundamental problem with the older approach – this has been revised in *VORLAX2024d*.

As with the thin panel, we consider the suction side Cp_{min} limit to be $Cp_{min} = 0.7\ Cp_{vac}$.

We must also limit the positive pressures. We must note that only under the pure incompressible (i.e., M=0) assumption does stagnation pressure equal the sum of the static pressure and the dynamic pressure. Whereas for calorically perfect compressible flow, the stagnation pressure does NOT equal the sum of the static and dynamic pressure, but rather:

$$p_{stag} = p_{static}\left(1 + \frac{\gamma - 1}{2} M_\infty^2\right)^{\frac{\gamma}{\gamma-1}}$$

Older versions of *VORLAX* defined the windward surface pressure limit at subsonic speeds as Cp_{stag}=+1.0, but at supersonic speeds considered the calorically perfect compressible flow stagnation pressure as the upper limit:

$$Cp_{stag} = \frac{\left(1 + \frac{\gamma - 1}{2} M_\infty^2\right)^{\frac{\gamma}{\gamma-1}} - 1}{\frac{\gamma}{2} M_\infty^2}$$

This leads to the code reporting clearly non-physical values for Cp_{stag} at high freestream Mach numbers. $Cp_{stag} >> 10$ at Mach 5; see TABLE 1.[14][15]

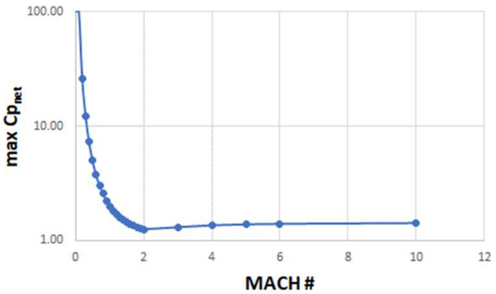

FIGURE 10 – $Cp_{net}max$ as a Function of Mach number.

TABLE 1 "*Ur-VORLAX*" limiting pressures as compared to *VORLAX2024* limited pressures.

	"Ur" VORLAX		VORLAX 2024	
MACH	Cpvac	Cpstag	70% Cpvac	Cpstag
0	-143.00	1.003	-100.00	1.000
0.1	-143.00	1.010	-100.10	1.000
0.2	-35.75	1.023	-25.03	1.000
0.3	-15.89	1.041	-11.12	1.000
0.4	-8.938	1.064	-6.256	1.000
0.5	-5.720	1.093	-4.004	1.000
0.6	-3.972	1.129	-2.781	1.000
0.7	-2.918	1.170	-2.043	1.000
0.8	-2.234	1.219	-1.564	1.000
0.9	-1.765	1.276	-1.236	1.000
1	-1.430	1.340	-1.001	1.276
1.1	-1.182	1.414	-0.8273	1.337
1.2	-0.9931	1.497	-0.6951	1.396
1.3	-0.8462	1.591	-0.5923	1.449
1.4	-0.7296	1.696	-0.5107	1.494
1.5	-0.6356	1.814	-0.4449	1.532
1.6	-0.5586	1.946	-0.3910	1.565
1.7	-0.4948	2.093	-0.3464	1.594
1.8	-0.4414	2.256	-0.3090	1.618
1.9	-0.3961	2.437	-0.2773	1.639
2	-0.3575	5.672	-0.2503	1.657
3	-0.1589	13.47	-0.1112	1.756
4	-0.0894	30.18	-0.0626	1.792
5	-0.0572	62.61	-0.0400	1.809
6	-0.0397	120.7	-0.0278	1.818
10	-0.0143	606.3	-0.0100	1.832

Following NACA 1135, [13] we believe that a more reasonable assumption is that any stagnating supersonic or hypersonic freestream flow will form an off-body shock. Thus, we may formulate the practical upper limit for stagnating pressure coefficients as:

$$Cp_{stag} = \frac{p_{o2} - p_\infty}{q} = \frac{\left[\left(1+\frac{\gamma-1}{2}M_2^2\right)^{\frac{\gamma}{\gamma-1}}\right]\left[1+\frac{2\gamma}{\gamma+1}(M_\infty^2-1)\ \right]-1}{\frac{\gamma}{2}M_\infty^2}$$

Where:

$$M_2^2 = \frac{1+\left[\frac{\gamma-1}{2}\right]M_\infty^2}{\gamma M_\infty^2 - \frac{\gamma-1}{2}}$$

This results in a Mach dependent trend which asymptotes to Cp_{stag} ~ +1.83 at the very highest freestream Mach numbers. [14] While we realize that the constant γ assumption is only formally valid for *M*<=5 in flight, we advocate that this revision will still produce better quality estimates of lift and drag than found using the original formulation.

D. Improving Solution Robustness at Supersonic Speeds

Miranda writes that “at supersonic Mach numbers, the velocity induced by a discrete horseshoe vortex becomes very large in the very close proximity of the envelope of Mach cones generated by the transverse leg of the horseshoe.” [2] To improve convergence stability, we will define “the characteristic surfaces by the equation $(x-x_1)^2 = C\,B^2\{(y-y_1)^2+(z-z_1)^2\}$ where C is a numerical constant whose value is greater than 1. “Ur-*VORLAX*” has C = 1/0.8; we leave this value unchanged for *VORLAX2024d*. If we change this constant upwards to *C*=1/0.7, we find that the solver will be less prone to numerically diverge. At the same time, the supposedly “converged” solutions become clearly non-physical and with irregular patches featuring strong negative *Cp*’s. At the present time, we leave the constant at its original value of *C*= 1/0.8 and accept the fact that the solver will not be unconditionally convergent at supersonic speeds – particularly when analyzing complex geometries featuring sandwich panels.

Miranda also notes that “another numerical problem, peculiar to the supersonic horseshoe vortex, exists in the planar case (field point in the plane of the horseshoe) when the field point is close to a transverse vortex leg swept exactly parallel to the Mach lines (sonic vortex), while the vortex lines immediately in front of and behind this sonic vortex are subsonic and supersonic, respectively.” [2] To improve convergence, *VORLAX* replaces the boundary condition equation and averages the circulation strength among neighboring vortices.

Careful benchmark studies found that global solution failures arose when the “sonic” field point was adjacent to either the leading-edge or trailing-edge. In this case, it is impossible for any algorithm to interpolate the circulation strength at this edge node. This limitation remains in *VORLAX2024d*.

At the same time, our benchmark studies found that global solution failures also arose because the existing interpolation algorithm was set to have an overly broad capture window. Successful interpolations may occur when a single chordwise field point needs to be approximated between two otherwise converged field points. To improve solution robustness, *VORLAX2024d* narrows the definition of when the swept transverse vortex leg “exactly” matches the Mach lines.

Consider an isolated swept and tapered wing, with a leading edge sweep of 60° and a trailing edge sweep of 41°; see FIGURE 11. For *M*<=1.32, both leading-edge and trailing-edge flows are subsonic; for 1.32<*M*<2.0 the leading-edge flow is subsonic but the trailing edge flow is supersonic; thus, interior field points may align with the “sonic” condition when the code is run at these freestream speeds. Above *M*>2.0, both leading-edge and trailing-edge flows are supersonic; it is impossible for any gridding to result in transverse vortex legs aligning with sonic flow conditions.

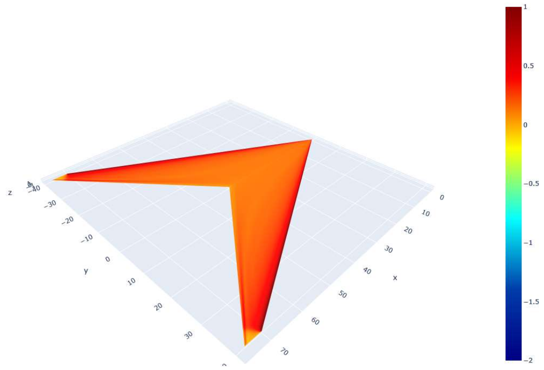

FIGURE 11 – Isobar Pattern of Supersonic Test Wing M=1.36, α=4° , β=1°.

TABLE 2 – Comparison of *VORLAX2024d* with respect to earlier compiles showing improvement in convergence of supersonic flow geometry.

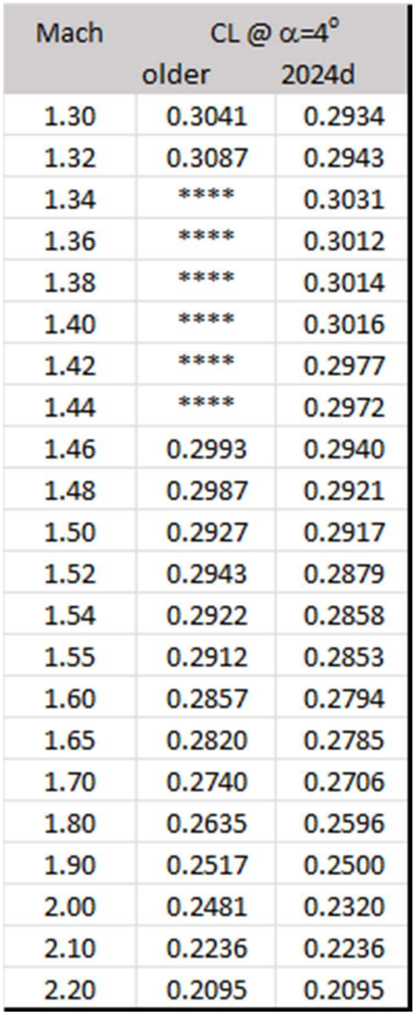

Mach	CL @ α=4°	
	older	2024d
1.30	0.3041	0.2934
1.32	0.3087	0.2943
1.34	****	0.3031
1.36	****	0.3012
1.38	****	0.3014
1.40	****	0.3016
1.42	****	0.2977
1.44	****	0.2972
1.46	0.2993	0.2940
1.48	0.2987	0.2921
1.50	0.2927	0.2917
1.52	0.2943	0.2879
1.54	0.2922	0.2858
1.55	0.2912	0.2853
1.60	0.2857	0.2794
1.65	0.2820	0.2785
1.70	0.2740	0.2706
1.80	0.2635	0.2596
1.90	0.2517	0.2500
2.00	0.2481	0.2320
2.10	0.2236	0.2236
2.20	0.2095	0.2095

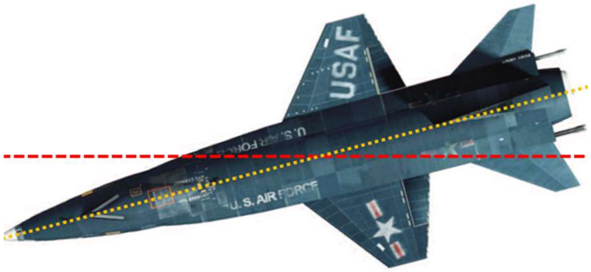

FIGURE 12 – Comparison of Wind vs. Body Aligned reference frames in Sideslip.

Turning to TABLE 2, we can examine the differences in solution arising from changing the width of the interpolation capture window. Below M<=1.32, the two compiles produce solutions which match to two significant figures (the slight reduction in lift arising from the imposition of the limiting algorithm on *Cpnet)*. Above M>=2.0, both older and newer compiles produce solutions which match to four significant figures. In the critical region between 1.32<M<2.0, we find six examples where the older compile produced divergent solutions; in *VORLAX2024d* solutions were converged for all considered Mach numbers. In this region, we see that the solutions do differ from each other in the third significant figure. Returning to FIGURE 11, which is for the test wing at M=1.36 (a speed which led to numerical divergence in the earlier compiles) we may note the smooth and plausible isobar patterns.

In Section V we will discuss how grid-density impacts solutions at transonic and supersonic speeds.

E. Dihedral Effect Inconsistencies due to Surface Pressure Integration Strategies and Double-Accounted Empirical Corrections

Benchmark modelling of the long and slender North American X-15 configuration revealed an issue with how the original version of *VORLAX* integrated surface pressures into rolling moments. Older versions of *VORLAX* ostensibly integrated surface pressures into aggregate forces and moments in the "wind axis." [2] In fact, the code integrated surface pressures through a double nested loop, first integrating all chordwise stations at a given spanwise location into a net force and then integrating each spanwise strip into the total panel load and moment.

While this strategy might have sufficed for a high aspect ratio wing, the X-15 with its aerodynamics dominated by the slender fuselage can only use this approach if the code integrates surface pressures into body axis. We can see from FIGURE 12 that in the wind axis a sufficiently yawed airframe can have all forebody pressures (both left and right of the line of bilateral symmetry) act to roll the aircraft in the same direction whereas all afterbody pressures (both left and right of the line of bilateral symmetry) act to roll the aircraft in the opposite direction. Thus, we see that the integration scheme internal to the original *VORLAX* algorithm was poorly conceived to handle this sort of geometry. In *VORLAX2024d*, the pressure integrations have been revised to directly render forces and moments into a bod*y*-aligned axis.

After extensive calibration work, it became evident that the skewed vortex correction term, *SICPLE*, was over-accounted for in all prior versions of *VORLAX*. [2] *VORLAX2024d* reduces the magnitude of the *SICPLE* correction by a factor of 3; this greatly improves its ability to benchmark the dihedral effect ($dCl/d\beta$) from wind tunnel tests of a wide variety of aerodynamic configurations. It is clear why Miranda added the *SICPLE* correction; absent the "adjustment," the stability axis $dCl/d\beta$ vs α trend for a swept wing configuration does not increase in magnitude as it should; see FIGURE 13. We will show over the rest of the paper that the revised *VORLAX* produces estimates of $dCl/d\beta$ consistent with wind tunnel results.

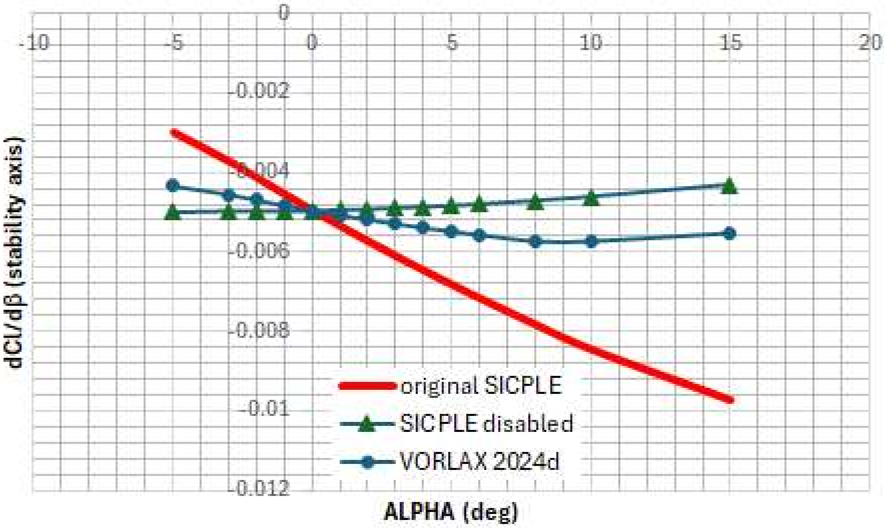

FIGURE 13 – Comparison of Dihedral Effect Predictions for a generic Swept Wing Airliner Configuration.

F. Revised Stability Axis Transformation

Once the forces and moments have been integrated up in body-aligned axis about the specified moment reference point, *VORLAX2024d* will render them into other modern engineering reference frames using the following transformation equations: [10]

$$
\begin{aligned}
CL_{STAB} &= CN_{BODY} * cos(\alpha) - CA_{BODY} * sin(\alpha)\\
CD_{STAB} &= CA_{BODY} * cos(\alpha) + CN_{BODY} * sin(\alpha)\\
CD_{STAB} &= CD_{BODY} * cos(\Psi) - CY_{BODY} * sin(\Psi)\\
CY_{STAB} &= CY_{BODY}\\
CM_{STAB} &= CM_{BODY}\\
CRM_{STAB} &= CRM_{BODY} * cos(\alpha) + CYM_{BODY} * sin(\alpha)\\
CYM_{STAB} &= CYM_{BODY} * cos(\alpha) - CRM_{BODY} * sin(\alpha)
\end{aligned}
$$

G. Suppression of Results from Poorly Converged Solutions

The earlier versions of *VORLAX* output aerodynamic coefficients regardless of the state of solution convergence. If *VORLAX2024d* detects a failure to converge, it will now supersede all output values with -999. When testing this compile, we discovered that existing input files representing large, complex models may have had *ITRMAX* set to 99 or below. Although the matrix was stable, 99 iterations proved insufficient to fully converge the solution. If *ITRMAX* was set to permit all solutions to fully converge, *VORLAX2024d* pressure field solutions agreed with earlier compiles to the fourth significant figure.

IV.Comparison of Results Between older *VORLAX* compiles and *VORLAX2024d*

A. Incompressible Sandwich Panel Pressures Over an Unswept AR6 Wing with a 0012 Airfoil

Let us begin our comparison of *VORLAX2024d* with prior versions by considering a solution which should not fundamentally change; that over a NACA 0012 finite wing at incompressible speeds. [16] We panel up an aspect ratio 6 untapered ("Hershey bar planform") wing using *VORLAX* sandwich panels and the 0012 thickness form.

When we run both *VORLAX2024d* alongside earlier versions of *VORLAX* we see no change in the total integrated lift coefficient, all solutions match (as we expect) to at least five significant figures, i.e., *CL*=0.63152 at α=10º.

Turning next to interrogate the solution more closely, we can see the upper surface *Cp* contours of the wing; see FIGURE 14. The solution displays the expected smooth isobar pattern with peak suction clustered at the upper surface leading edge. Spanwise pressure relief near the wing tips is equally evident.

In FIGURE 15, we can see the centerline *Cp* distribution between *VORLAX2024d* and *VORLAX2020*. These pressure coefficients also match each other to five significant figures. They exhibit the expected pattern of having stagnation (*Cp*=+1.0) on the lower surface just aft of the geometrical leading edge, and peak suction on the upper surface.

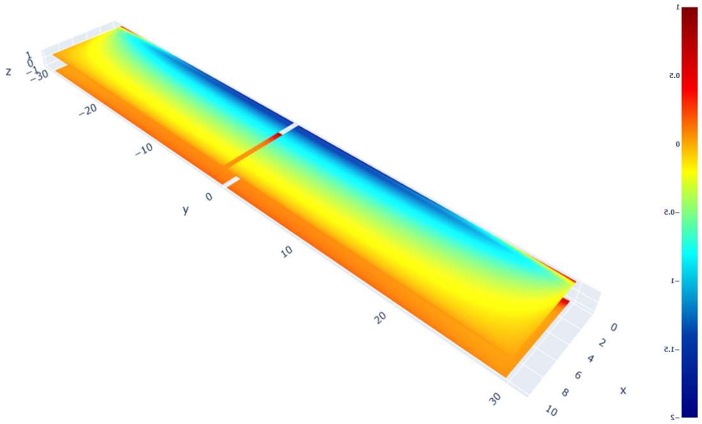

FIGURE 14 - NACA 0012 – *M*=0 (incompressible) at α=10-deg. Upper Surface *Cp* contours from a *VORLAX2024d* solution.

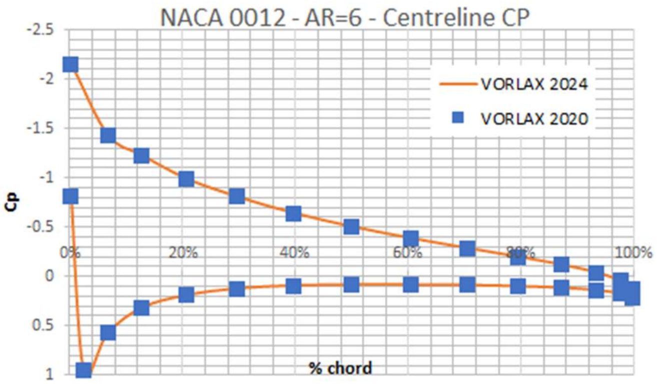

FIGURE 15 - NACA 0012 – *M*=0 (incompressible) at α=10-deg. Centerline *Cp* traces from *VORLAX2024d* and *VORLAX2020*.

B. Supersonic Sandwich Panel Pressures Over an Unswept AR3 Wing with a 6% Biconvex Airfoil

Let us continue our comparison of *VORLAX2024d* with prior versions by considering a second solution which should also not fundamentally change. That being flow over a 6% thick biconvex finite wing at supersonic speeds. [17] We panel up an aspect ratio 3 untapered ("Hershey bar planform") wing using *VORLAX* sandwich panels and a 6% biconvex form.

Once again, when we run both *VORLAX2024d* alongside earlier versions of *VORLAX* we see little change in the total integrated lift coefficient, we see *CL*=0.188 for *VORLAX2020* and *CL*=0.186 for *VORLAX2024d*. When we more closely interrogate the solution, we see that the essential vortex strengths are unchanged between the two versions of the code. The upper surfaces *Cp* distribution shows the expected "Mach Cone" pattern emanating from the leading edge of the wing tips; see FIGURE 16.

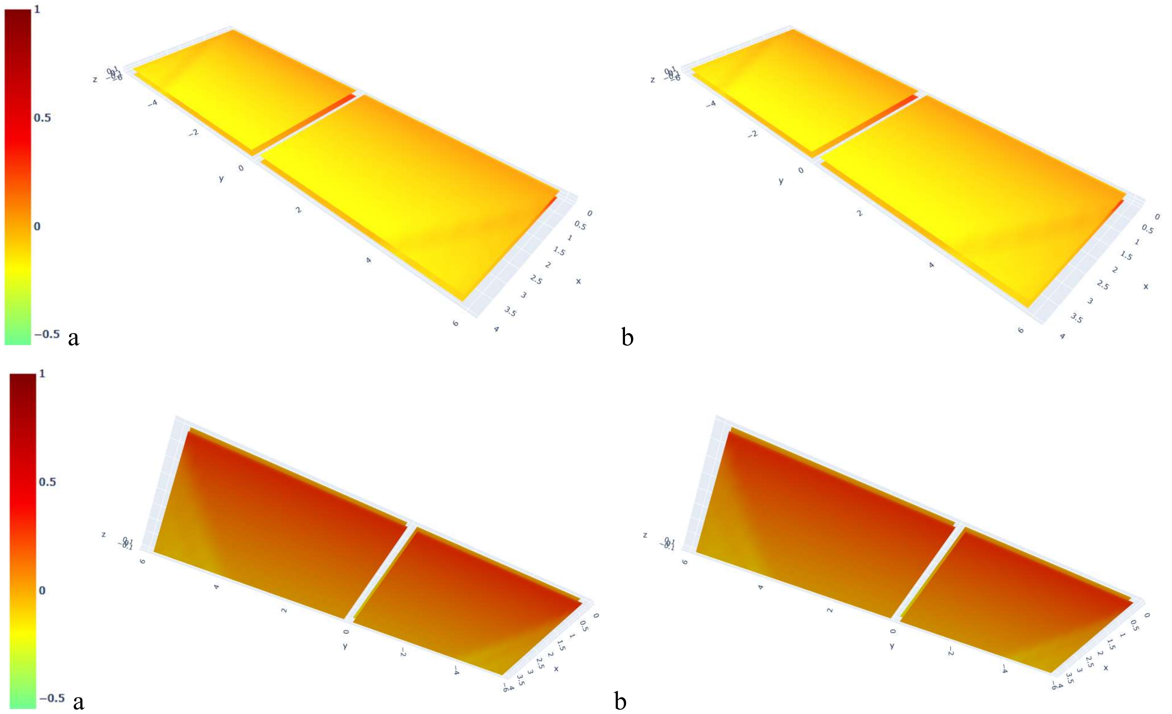

FIGURE 16 - 6% Biconvex AR=3 @ *M*=2 *α*=5-deg – *NVOR*=20/*RNCV*=50 a) Upper Surface *Cp* contours *VORLAX* 2020, b) Upper Surface *Cp* contours *VORLAX2024d*, c) Lower Surface *Cp* contours *VORLAX* 2020, d) Lower Surface *Cp* contours *VORLAX2024d*.

In FIGURE 17, we can see the centerline *Cp* distribution between *VORLAX2024d* (the line) and *VORLAX2020* (the symbols). For both upper and lower surfaces, these pressure coefficients match each other to 5 significant figures. They exhibit the expected pattern of lacking any identifiable stagnation pressure on the surface. The solutions are essentially identical because neither engages the pure vacuum *Cpmin* limit from *VORLAX2020* (*Cpmin*=*Cpvac*=-0.3575) or the 70% vacuum limit from *VORLAX2024d* (*Cpmin*=0.7*Cpvac*=-0.2550).

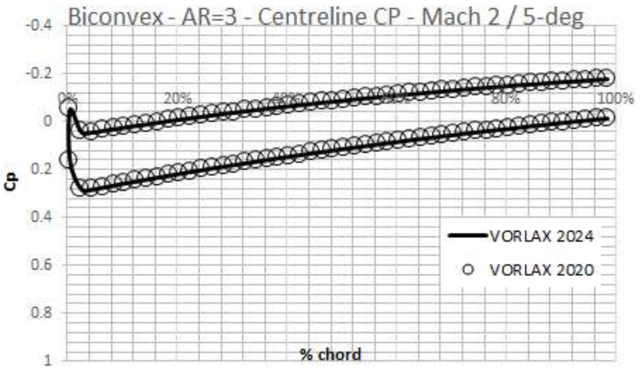

FIGURE 17 - 6% Biconvex AR=3 @ M=2, α=5-deg – Centerline *Cp* trace – *NVOR*=20/*RNCV*=50 grid.

C. Hypersonic Sandwich Panel Pressures Over an Unswept AR6 Wing with a Wedge Airfoil

Little has been written about the use of *VORLAX* sandwich panels at hypersonic speeds. The formulation is fundamentally different from a quasi-Newtonian code and its results will document more subtle flow features that can be lost with impact angle approximations; the wedge airfoil proves a suitable example. [18]

Now, let us consider the flow over a 10-degree wedge wing with an aspect ratio of 3 with a untapered ("Hershey bar planform") wing using *VORLAX* sandwich panels. When we run both *VORLAX2024d* alongside earlier versions of *VORLAX* we see little change in the total integrated lift coefficient, we see at Mach=5 and α =10-deg CL=0.27194 for both *VORLAX2020* and *VORLAX2024d*. Upper surface (leeward) pressures are essentially zero for both solutions, neither engages either the pure vacuum *Cpmin* limit from *VORLAX2020* (*Cpmin*=*Cpvac*=-0.0572) or the 70% vacuum limit from *VORLAX2024d* (*Cpmin*=0.7 *Cpvac*=-0.0400). Windward side *Cp*'s are essentially constant; they are dominated by uniform turning of the flow by the flat windward surface; see FIGURE 18. As with the supersonic case, we do see a minor "Mach Cone" disturbance emanating from the leading edge of the wing tips; see FIGURE 19.

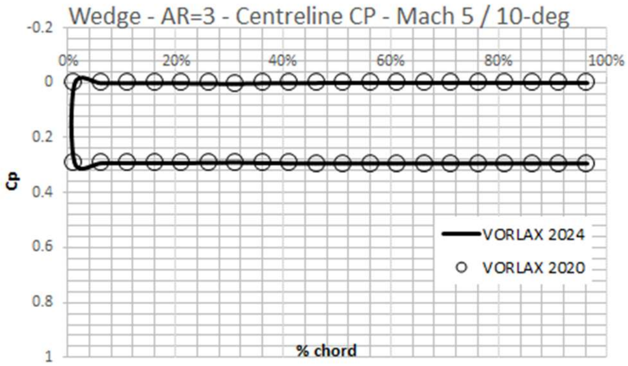

FIGURE 18 - 10-deg Wedge AR=3 @ *M*=5, α=10-deg – Centerline *Cp* trace

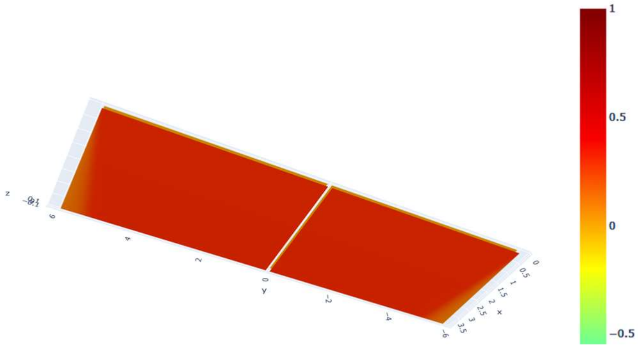

FIGURE 19 - 10-deg Wedge AR=3 @ *M*=5, α=10-deg – Lower Surface (Windward side) *Cp* contours from *VORLAX2024*.

D. Hypersonic Sandwich Panel Pressures on a Swept Wing Body Configuration

My collaborator Wu discovered the need to restrict *Cpstag* when developing a supersonic sandwich panel model of a highly swept wing body configuration. This geometry with a 0.4% *t/c* leading edge radius, swept wing that includes spanwise variation in both camber and washout, presented concerning results.

When run at Mach 5, α=10-deg, *VORLAX2020* generated a positive *Cp*'s at the most forward integration point greatly in excess of expectations (*Cpmax* >> 2, in this case *Cpmax*=+6.39); see FIGURE 20. In reality, the finite leading-edge radius leads to the formation of a detached shock wave which supports the more classical limitation to *Cpstag* ~ + 1.85.

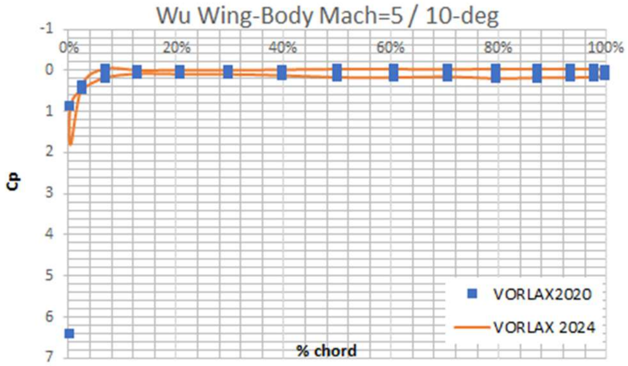

FIGURE 20 - Complex Swept Configuration @ *M*=5, α=10-deg. *Cp* trace on the inboard main wing.

We quickly realized that the presence of these artifacts near the leading edge greatly impacted the overall solution. Under *VORLAX2020*, *CL*= 0.1006 and *Cm*=-0.18017; whereas with *Cpstag* limited *VORLAX2024d* estimates *CL*=0.1663, *Cm*=-0.21722. This represents a substantial change in lift and moments, a discrepancy of as much as 60% in lift; this certainly cannot be ignored.

At the same time, the overall solutions are otherwise extremely similar. Refer to FIGURE 21 to compare the upper and lower surface pressure distributions for the two solutions. With the exception of the leading-edge pressures, the solutions are otherwise identical to one another. This highlights the very real power given by a few node-points in a CFD solution to massively steer the values of integrated forces and moments.

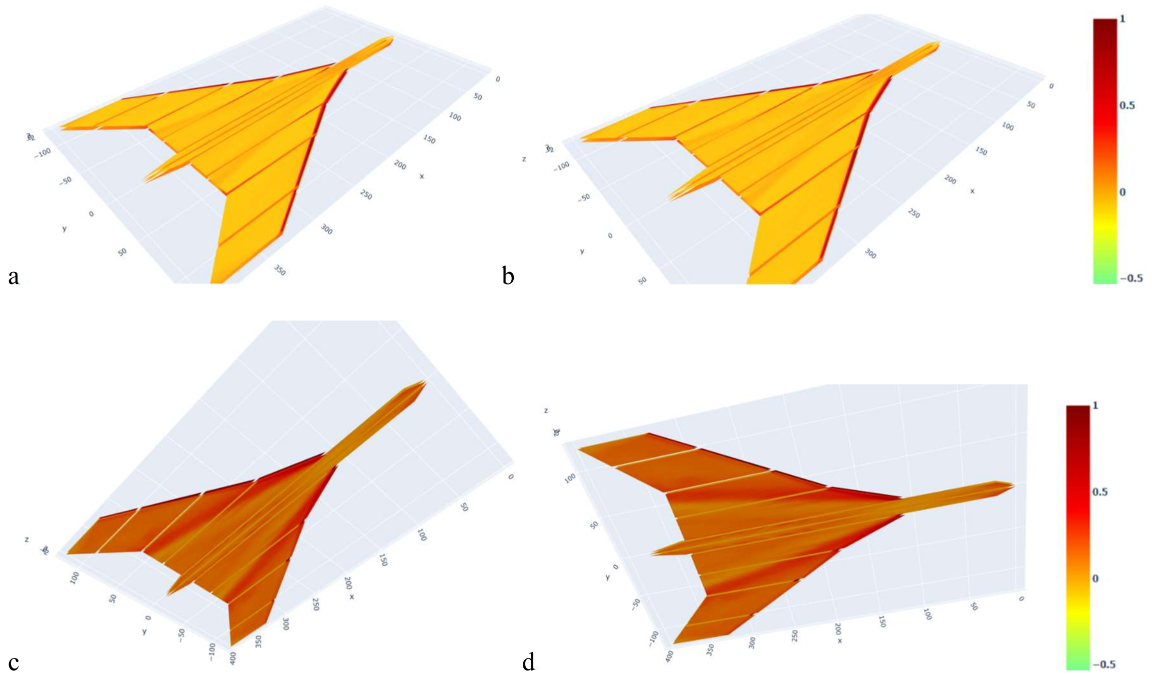

FIGURE 21 – Complex swept, cambered, twisted wing-body configuration @ Mach 5 α=10-deg – a) Upper Surface *Cp* contours *VORLAX* 2020, b) Upper Surface *Cp* contours *VORLAX2024d*, c) Lower Surface *Cp* contours *VORLAX* 2020, d) Lower Surface *Cp* contours *VORLAX2024d*.

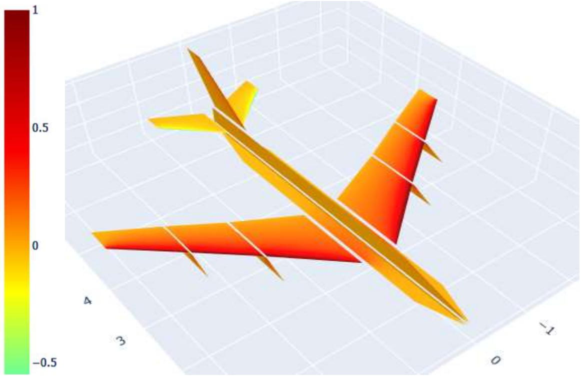

FIGURE 22 – Net *Cp* across thin flat plate model of the Subsonic Transport Aircraft from NASA TM X-1345 at Mach 0.4, α=6-deg, β=1-deg.

E. Aerodynamic Stability of a Subsonic Transport Aircraft

This section highlights how the changes in *SICPLE* improve correlation with the predicted dihedral effect of a complete configuration. The geometry found in NASA TM X-1345 is of a four-engine, swept wing subsonic transport reminiscent of a Boeing 707. [19] As this wind tunnel test is from later in the 1960's, the facility has been upgraded to obtain sideslip data over a wide range of attitudes. As before, we model the configuration in *VORLAX* using purely thin flat panels; we may run the solution at a variety of speeds and attitudes; see FIGURE 22.

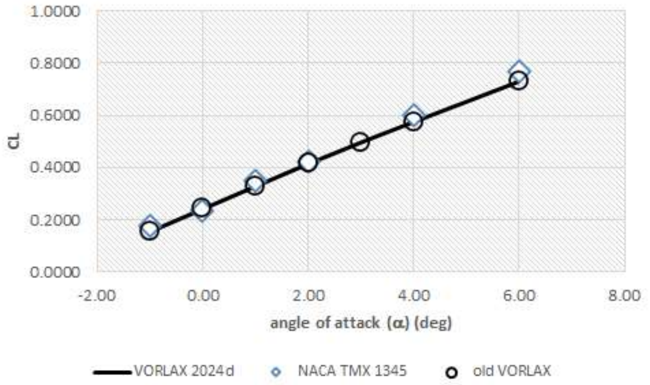

FIGURE 23 – Lift Coefficient (*CL*) of Subsonic Transport aircraft at Mach 0.4. [19]

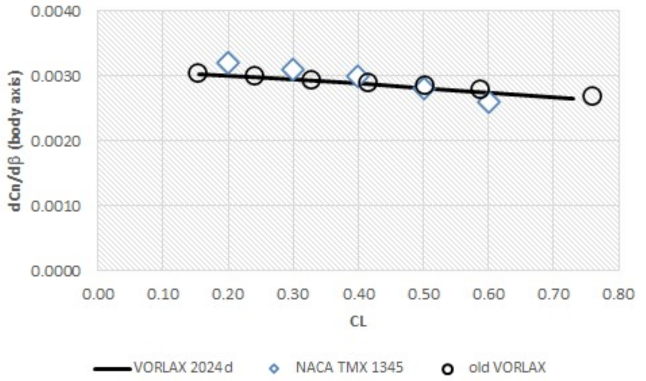

FIGURE 24 – Body Axis Directional Stability (*dCn/dβ*) of Subsonic Transport aircraft at Mach 0.4. [19]

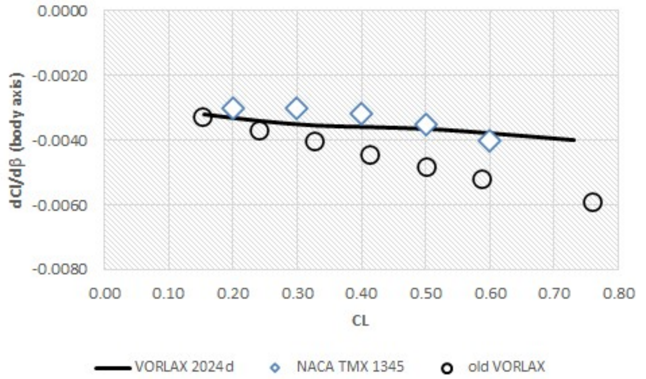

FIGURE 25 – Body Axis Dihedral Effect (*dCl/dβ*) of the Subsonic Transport Aircraft at Mach 0.4. [19]

In FIGUREs 23, 24 and 25 we compare old *VORLAX* and *VORLAX2024d* solutions against purely subsonic wind tunnel data; i.e., at Mach 0.4. [19] Once again, we see a solid agreement between wind-tunnel body-axis and *VORLAX* body-axis results for lift coefficient (*CL*), weathercock stability (*dCn/dβ*) and dihedral effect (*dCl/dβ*) across a range of angles-of-attack.

FIGURE 23 demonstrates how all versions of *VORLAX* accurately capture the lift coefficient trend found in the wind tunnel. *VORLAX2024d* solutions are identical to the earlier *VORLAX* compiles at low angles of attack and differ in the second significant figure at α=6°. This is because the *VORLAX2024d* compile limits the maximum net suction across a node point; this limitation begins to impact the differential pressures developed at the leading edge of the wing.

FIGURE 24 demonstrates how all versions of *VORLAX* accurately capture the directional stability of the Boeing 707 as measured in the wind tunnel. *VORLAX2024d* solutions match the earlier *VORLAX* compiles to two significant figures at all conditions. They both match wind tunnel, differing by no more than 5%.

FIGURE 25 demonstrates how the revised *SICPLE* correction more accurately matches the dihedral effect found in wind tunnel data for conventionally configured aircraft at subsonic speeds. *VORLAX2024d* captures both the magnitude of and trend (increasing dihedral effect with increasing lift coefficient) whereas the earlier version of *VORLAX* substantially overpredicts the effective dihedral.

Thus, when used for preliminary design purposes, the older version of *VORLAX* would tend to predict a vehicle with faster Dutch Roll frequencies and worse cross-wind trim performance than would be indicated by the wind tunnel. The revisions in *VORLAX2024d* considerably improve the quality of its results when used to model flight dynamics problems.

F. Basic Aerodynamic Stability of the Bell X-1A

This section highlights how the changes in integration axis alter the predicted dihedral effect of complete configurations. Aircraft with dorsal vertical tails and/or swept wings typically display a trend where their dihedral effect (*dCl/dβ*) becomes increasingly powerful with rising angle-of-attack. The straight wing Bell X-1/X-1A is a good example of a real-world wing/body/tail configuration with some wind tunnel and extensive flight-test data. Here, we model the configuration in *VORLAX* using purely thin flat panels; we may run the solution at a variety of speeds and attitudes; see FIGURE 26.

In FIGUREs 27 and 28 we compare the *VORLAX2020* and *VORLAX2024d* results at both incompressible and supersonic speeds against wind Tunnel data. [20][21] Sadly, due to facilities limitations, lateral-directional data is limited to zero angle-of-attack. Nonetheless, within limits, we see an excellent agreement between tunnel and *VORLAX* for both static directional and dihedral effect at incompressible (Mach=0 for *VORLAX*, Mach=0.4 for the Wind Tunnel) and supersonic (Mach=2.0 for *VORLAX*, Mach=1.92 for the Wind Tunnel) speeds.

VORLAX shows the clear degradation in static directional stability with increasing supersonic speeds. The surface pressure limitations and integration differences and *SICPLE* changes between *VORLAX2020* and *VORLAX2024d* somewhat change the estimated stability. For example, at M=2 and α=10-deg, *VORLAX* 2020 estimates *dCn/dβ*=+0.0174 whereas *VORLAX2024d* predicts +0.0134; a reduction of ~20%.

The difference in estimated dihedral effect between *VORLAX2020* and *VORLAX2024d* is even more marked; especially as the angle-of-attack increases. This is due to the revisions for this body dominated problem, the earlier compiles predict a substantially stronger amount of roll-due-to-yaw than obtained with the revised integration scheme. While FIGURE 28 demonstrates a material change in predicted aerodynamic coefficients, with this limited dataset it cannot adjudicate which formulation is more or less "correct."

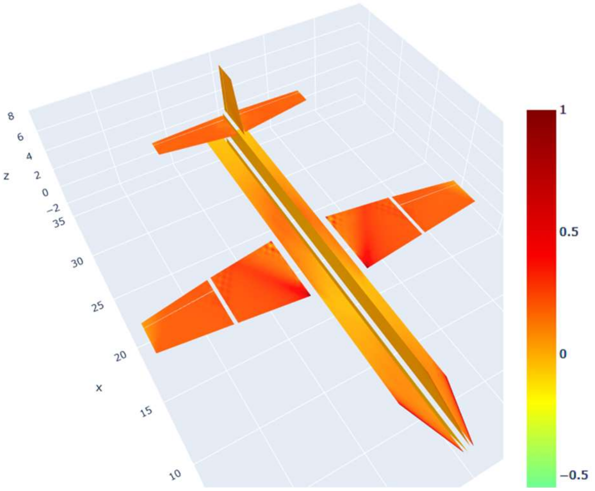

FIGURE 26 - Net *Cp* across thin flat plate model of the Bell *X*-1A – Mach 2.0 α=5-deg, β=1-deg.

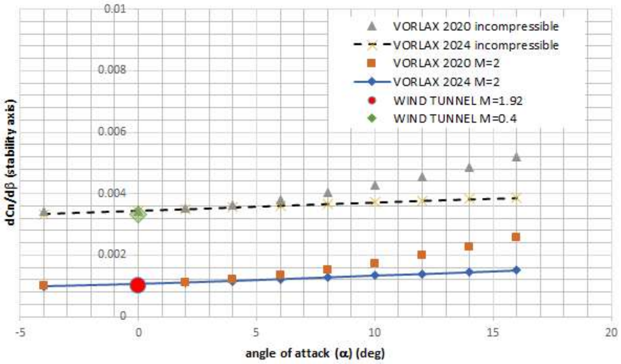

FIGURE 27 – Stability Axis Directional Stability (*dCn/dβ*) of the Bell *X*-1 as measured in the wind tunnel and modelled with old *VORLAX* and *VORLAX2024d*. [20][21]

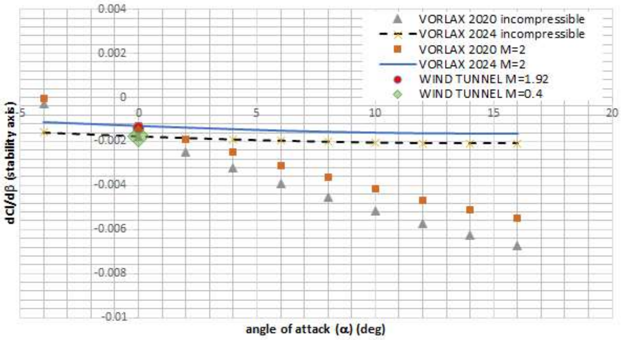

FIGURE 28 – Stability Axis Dihedral Effect (*dCl/dβ*) of the Bell *X*-1 as measured in the wind tunnel and modelled with old *VORLAX* and *VORLAX2024d*. [20][21]

G. Basic Aerodynamic Stability of the North American X-15

This section highlights how the changes in integration axis alter the predicted dihedral effect of complete configurations. The North American X-15 is another high-speed configuration with considerable published wind tunnel and flight-test data availability.

Compared to our earlier modes, we slightly revised the fuselage geometry to better reflect our understanding of the "as flown" X-15 dimensions. The center of gravity has been moved back from being near the wing-fuselage junction to a location 20% of the mean geometric chord length aft of the wing-fuselage junction; while this might not exactly reflect flight – this better reflects the moment reference point NASA engineers used to produce the published wind tunnel data.

This study shows the early "as flown" X-15 configuration with the large ventral fin; see FIGURE 29. We may note the slight asymmetry in pressure fields between the left-hand and right-hand wing and chines. For this configuration, the asymmetry in lift between the chines contributes to the effective dihedral as does the asymmetry in lift between the wings.

For this paper we consider a hybrid *VORLAX* model where the fuselage and wings are modelled as thin flat panels, but the distinctive "wedge" vertical tail is modelled as a sandwich panel. FIGURE 30 documents the effect tail paneling strategy has on the aerodynamic predictions. We may model the wedge shaped vertical tail first as a simple, flat panel or as a "sandwich panel" wedge. Because of *Cpvac* and *Cpmax* limits, a flat panel model will have limited ability to generate restoring moments at hypersonic speeds. Recall that at Mach 6, a 70% vacuum effectively neutralizes any "lifting" capability from the leeward surface of a thin wing. At high Mach numbers, the wedge airfoil dorsal and ventral fins with two windward surfaces proves much more effective in reality than a thin fin ever could.

We can see in FIGURE 30a that vertical tail paneling strategy does not impact lift coefficient with respect to angle-of-attack.

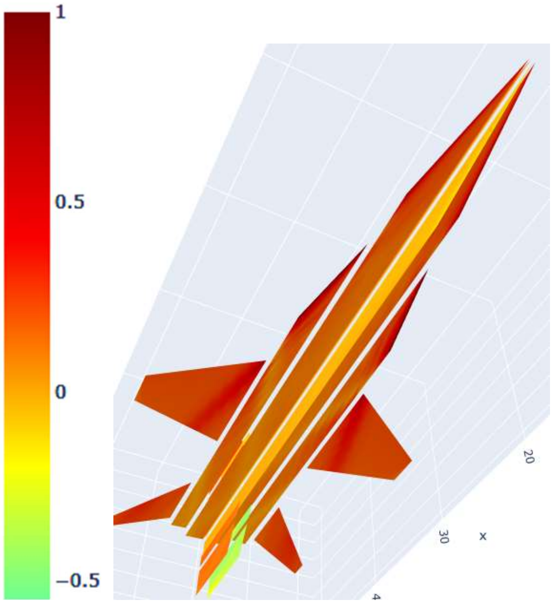

FIGURE 29 – Windward side view of North American X-15 (early config) – Mach 5.0 α=15-deg, β=5-deg.

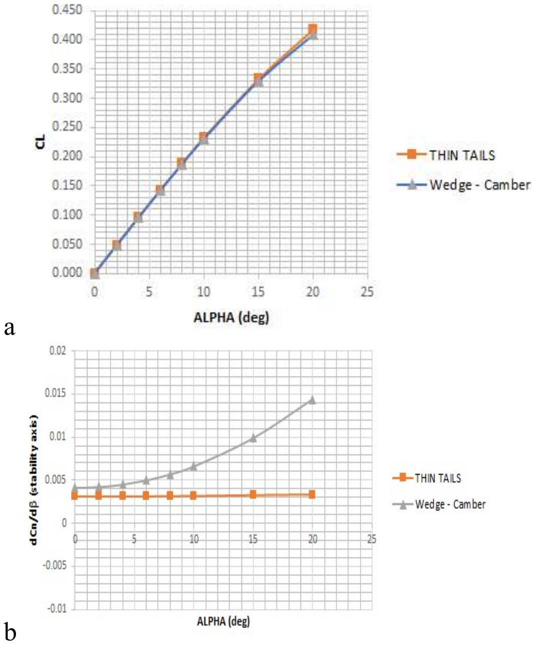

a

b

FIGURE 30 – X-15 *VORLAX* vertical tail modelling strategy comparing results for Thin and "Sandwich Panel" wedge tails. a) *CL* vs α, b) impacts on lateral/directional stability; *dCn/dβ* vs α. *VORLAX2024d* run at Mach=6.

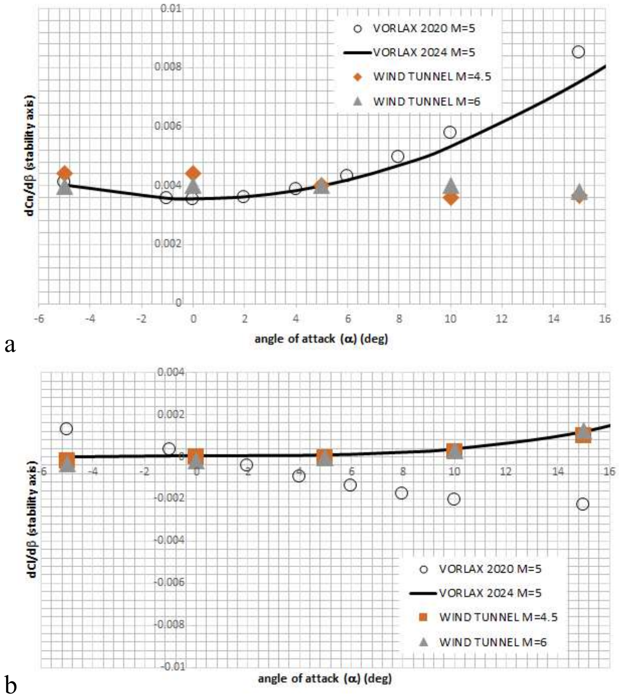

FIGURE 31 – Stability Benchmark – a) Directional Stability (*dCn/dβ*) and b) Dihedral Effect (*dCl/dβ*) of the North American X-15 (early config) as measured in the wind tunnel and modelled with *VORLAX* with a sandwich panel wedge dorsal and ventral fin.

We also see in FIGURE 30b that wedge airfoil vertical tail substantially alters the predicted directional stability. At Mach 6, the wedge tail configuration should and does develop much more side force due to sideslip than does the thin fin model. This leads to the corresponding increase in directional stability (*dCn/dβ*).

In FIGUREs 31a and b we compare the *VORLAX* 2020 to the 2024d compile against wind tunnel data. [22] We see a solid agreement between tunnel and *VORLAX* for both weathercock (*dCn/dβ*) and dihedral effect (*dCl/dβ*) across a range of angle-of-attack. We do note that both versions of *VORLAX* do tend to predict rising directional stability at higher angles of attack not seen in the wind tunnel data. *VORLAX2024d*, with all of its revisions, reduces the discrepancy with wind tunnel.

The biggest difference between the two solutions is found in the dihedral effect. The earlier *VORLAX* compile predicts a strong rise in effective dihedral as the angle-of-attack increases which is not seen in the wind tunnel data. *VORLAX2024d* with the reduced *SICPLE* correction closely matches wind tunnel data.

We can see how the *VORLAX2024d* upgrades improve correlation with wind tunnel, as they reduce both the predicted weathercock stability as well as the angle-of-attack dependence on the dihedral effect.

V. Grid Density Studies

A. Supersonic Sandwich Panel Pressures Over an Unswept AR3 Wing with a 6% Biconvex Airfoil

FIGURE 32 (overleaf) shows four identical supersonic sandwich panels at the same flight condition. For this geometry, the spanwise grid of the entire wing has a total of two times the *NVOR*, this is because the panel is mirrored about the x-z plane. While the chordwise grid equals just the number of *RNCV* points. The difference in solutions shown in FIGURE 32 comes from the number of chordwise and spanwise points; they all represent the identical geometry. Notice that FIGURE 32b has a checkerboarding pattern on the wing tip whereas the other solutions of the same basic geometry, but with different grid densities both coarser (FIGURE 32a) and finer (FIGURE 32c and FIGURE 32d) do not. This numerical anomaly tends to appear when the grid densities in front of particular nodes on the wing are too sparse. As the Mach number is changed, the number of nodes seen by other nodes in their respective Mach cone changes. When conditions are right, the checkerboarding pattern will appear. This is prone to happen when *NVOR* > *RNCV*. This can easily be remedied by increasing the number of *RNCV* points or by increasing both *NVOR* and *RNCV*. The danger of this numerical anomaly is that without a visualizer, the data resulting from checkerboarded wings is not necessarily unreasonable and will not throw a -999 in the output. Thus, additional care is needed when choosing the number of nodes for a sandwich panel at supersonic speeds.

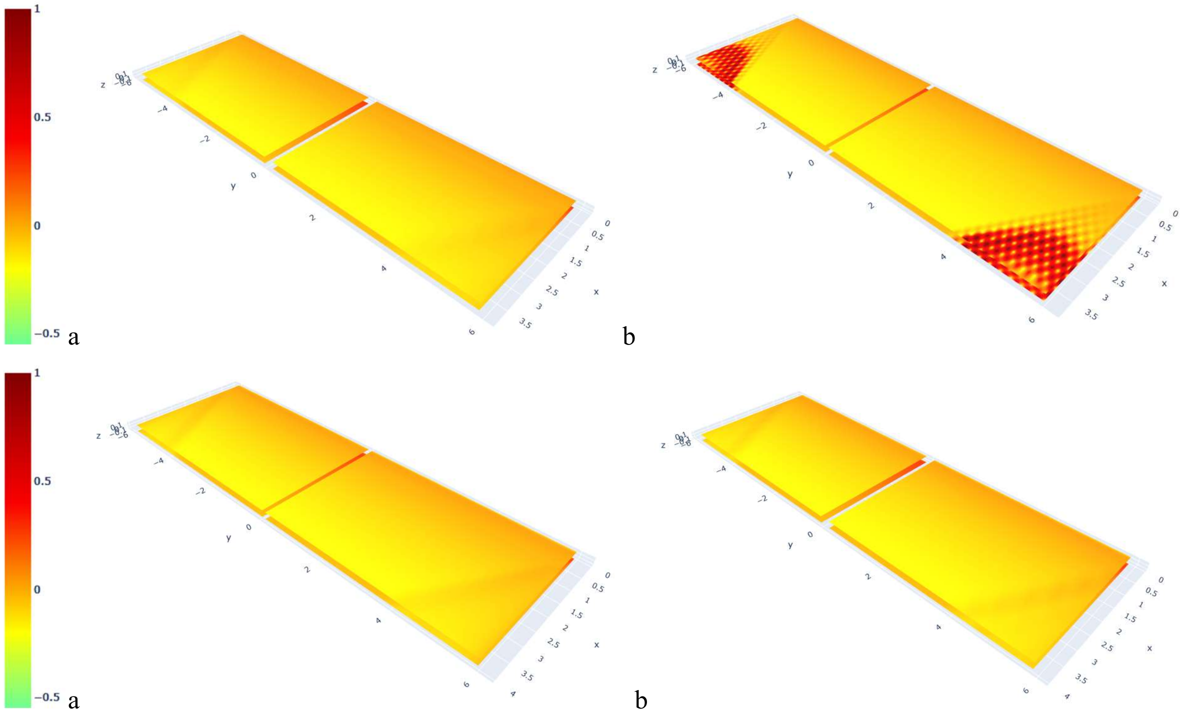

FIGURE 32 - 6% Biconvex AR=3 @ Mach 2 α=5-deg *VORLAX2024d* solutions – a) *NVOR*=20/*RNCV*=20, b) *NVOR*=50/*RNCV*=20, c) *NVOR*=50/*RNCV*=50, d) *NVOR*=20/*RNCV*=50.

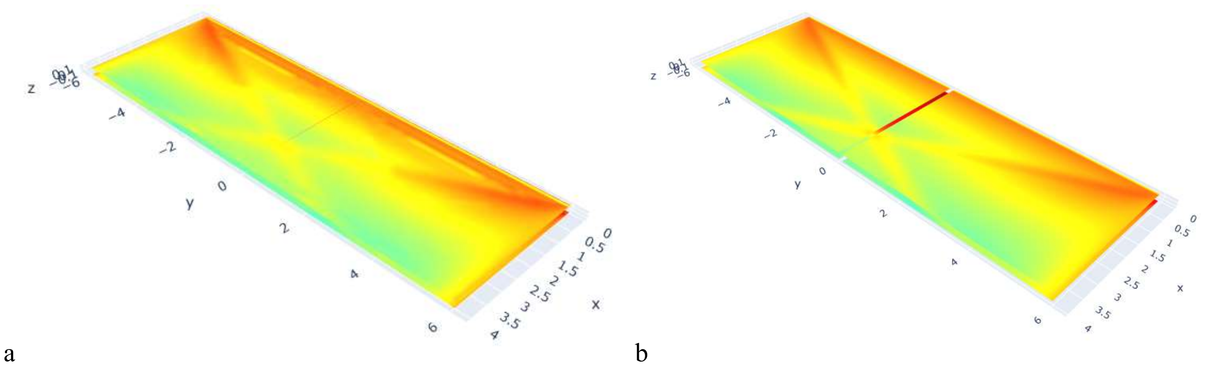

FIGURE 33 – 6% Biconvex AR=3 @ Mach 1.1 α=5-deg *VORLAX2024d* solutions – a) *LAX*=0, *LAY*=0 b) *LAX*=1, *LAY*=1.

Miranda originally implemented “linear” and “cosine” self-gridding functionality into *VORLAX*.[2] In the original code documentation, Miranda suggests that the user use “cosine” spacing in the chordwise direction to improve the quality of the solution. [2] He also claimed little difference in the accuracy between the spacing methods in the spanwise direction. [2] We have found this advice counterproductive when used supersonic sandwich panels. Linear spacing in both directions (*LAX*=1, *LAY*=1) is desirable as strange artifacts, see FIGURE 33, might appear in the pressure distribution. This often results in nonsensical pressure spikes and curved stratification. We believe that this is due to how crowded leading edge / trailing edge and wing-tip node points interacting with one another in a solution which should develop a simple striation along Mach cone lines.

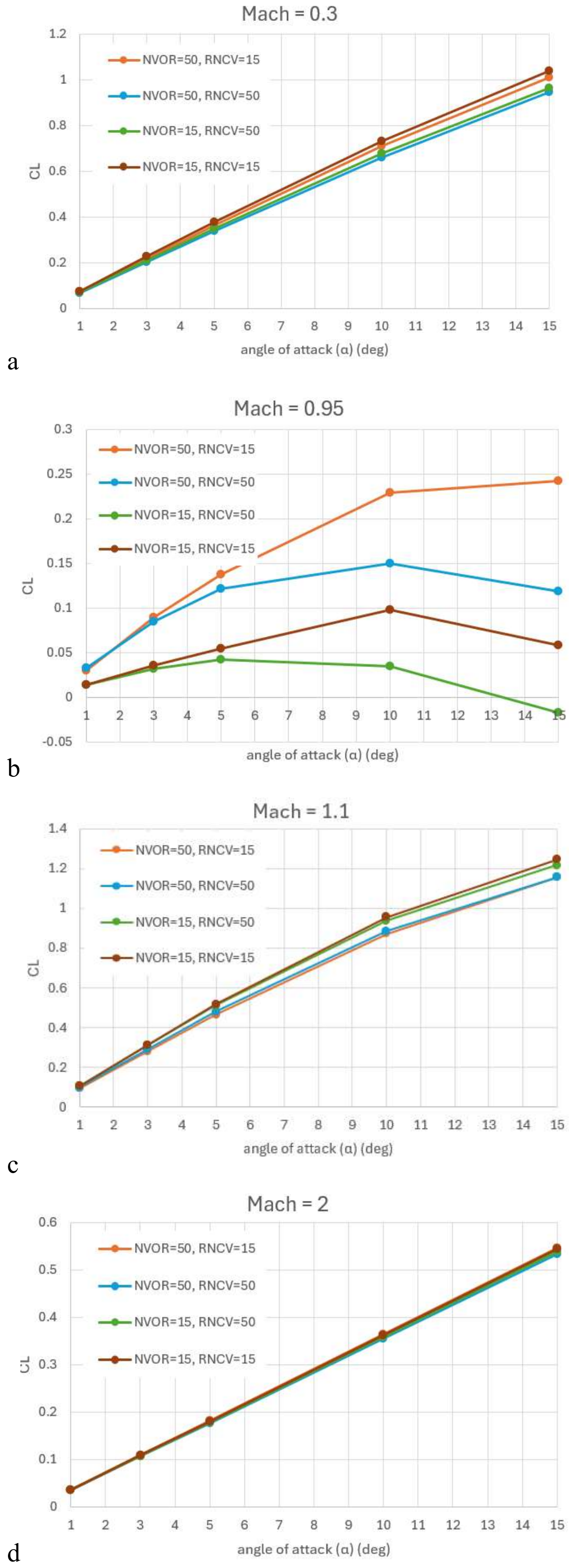

FIGURE 34 - 0012 Airfoil AR=6 at with panel spacing being the max chordwise thickness at a) M=0.3, b) M=0.95, c) M=1.1, d) M=2.0.

B. Transonic Sandwich Panel Pressures Over an Unswept AR6 Wing with a 0012 Airfoil

The first major consideration when gridding a sandwich panel is the number of points for the spanwise and chordwise distribution. Testing showed that the results are increasingly sensitive around sonic conditions. FIGURE 34 shows how large the discrepancy can get when nearly sonic; M=0.95 and M=1.1. But at this condition it is hard to say which, if any, of the *NVOR*/*RNCV* combinations are accurate. As *VORLAX* is incapable of representing shocks in places other than leading or trailing edges, results just below M=1 will diverge from reality. Thus, users of *VORLAX* must be aware of limitations of the theory, lest they wonder why the results change so much with grid density when they are in fact stretching the theory. It can be seen from FIGURE 34, besides the diverging case at M=0.95, the results are mostly indifferent to the grid density. So, if you keep in mind the risk of checkerboarding, the density is not a major factor.

The other major consideration unique to sandwich panels is the space between the upper and lower panels. Maranda found that “the results are not too sensitive to the magnitude of this gap; any value between one half to the full maximum chordwise thickness of the airfoil has been found to be adequate, the preferred value being two thirds of the maximum thickness.” [2] This still appears to be the case.

From FIGURE 35 (overleaf) it is clearly seen that the spacing does not make much of a difference. The following spacings between panels are looked at: a lazy method where space is 10% of the chord, the maximum chordwise thickness, and half the maximum thickness. With a thin, flat panel also shown as well to see the effects of the sandwich panel. Again, the M=0.95 should not be trusted for the same reasons mentioned above. Lastly the flat panel shows some difference; that is to be expected given it is a thin panel.

It is important to remember trailing vortices and how nodes will interact with one another. By following the techniques laid out by Martin [23] we can avoid other numerical anomalies. The major things to lookout for are first: chordwise nodes are not lined up, usually with the fuselage. This is seen in FIGURE 36 (overleaf) whereby breaking the fuselage into multiple a pieces better pressure distribution can be obtained. This numerical anomaly seems to appear in supersonic speeds and tends not to produce significant changes in overall force or moments.

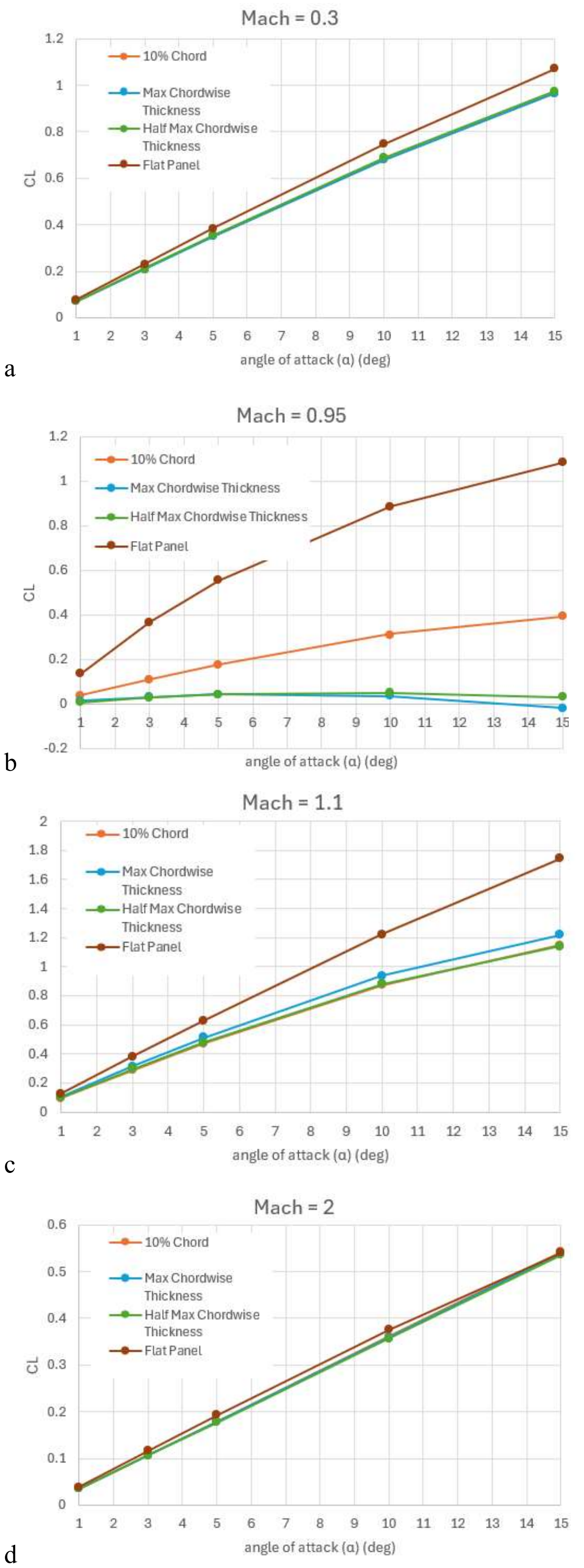

FIGURE 35 – 0012 Airfoil AR=6 *NVOR*=15 *RNCV*=50 at a) *M*=0.3, b) *M*=0.95, c) *M*=1.1, d) *M*=2.0.

The far more important interaction is how trailing vortices will interact with panels behind them. In the case seen in FIGURE 37, where the sandwich panel wing's trailing vortices interact with the sandwich panel horizontal tail, a nonsensical low-pressure streak forms in the converged solution. This can be fixed by cherry picking a non-anomalous *NVOR* on the horizontal tail, but that would need to be done at every Mach condition. It is best to avoid conditions where such interactions are possible as they are susceptible to producing "junk data;" which is not so clearly poorly converged to throw a "-999" error.

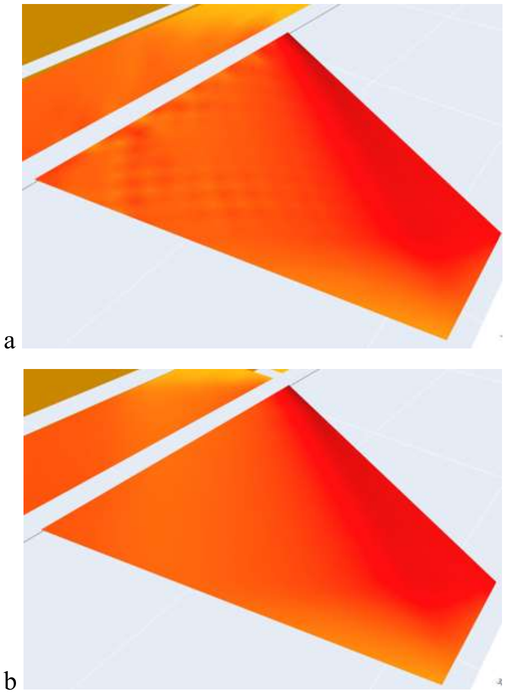

FIGURE 36 – Chordwise nodes a) not aligned b) aligned.

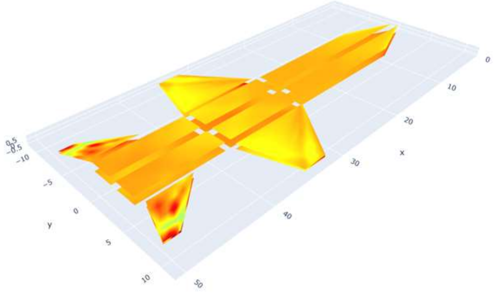

FIGURE 37 – X-15 sandwich panel geometry with numerical anomaly on horizontal tail.

VI. Historical Aircraft Verification Cases

At the dawn of supersonic aircraft design, supersonic wind tunnel test facilities had extremely small test section dimensions. As noted above in Section IV/F, the legendary Bell X-1 was configured without any available full configuration supersonic wind tunnel data; its final wind tunnel data set from 1947 was made at the Langley 8-ft "high-speed-tunnel," and did not exceed Mach 0.93. [24] At this point in time, with experience solely with straight-wing subsonic configurations, aerodynamic designers did not understand the flight dynamics implications of angle-of-attack dependencies in directional stability (*dCn/dβ*) and dihedral effect (*dCl/dβ*). During its flight test program "the Bell X-1A was found to have some highly undesirable handling qualities. In the vicinity of Mach number 2, the airplane commenced rolling uncontrollably." [21][25][26][27] In an attempt to better understand the problem, additional wind tunnel tests were performed at the in the Langley 9-inch supersonic tunnel at speeds up to Mach 2.62. While Langley evaluated the complete aerodynamic configuration they continued to be restricted to test "through an angle-of-attack range at zero yaw angle and through an angle-of-yaw range at zero angle-of-attack." [21]

It was not until later in the 1950's that the Langley tunnels were retrofitted with more complex sting systems that could render a pitch polar at a specified sideslip angle. [28] At this point, the wind tunnel community had realized that α and β combinations could be obtained by simultaneously pitching and rolling the model. Henceforth, wind tunnel data reports could document how directional stability (*dCn/dβ*) and dihedral effect (*dCl/dβ*) varied with Mach number and incidence (α). These post 1956 supersonic datasets prove of great interest as a source of validation data for the supersonic vortex lattice code. In this paper we showcase *VORLAX2024d* validation with wind tunnel data collected for the Bell X-1E, [29] the Bell X-2 [30], the Avro CF-105 prototype [31], a developmental configuration leading to the production F-104 [32], an early version of the Lockheed Blackbird [33], the Convair B-58 [34], a generic tactical fighter [35], and a developmental configuration of the North American X-15. [22]

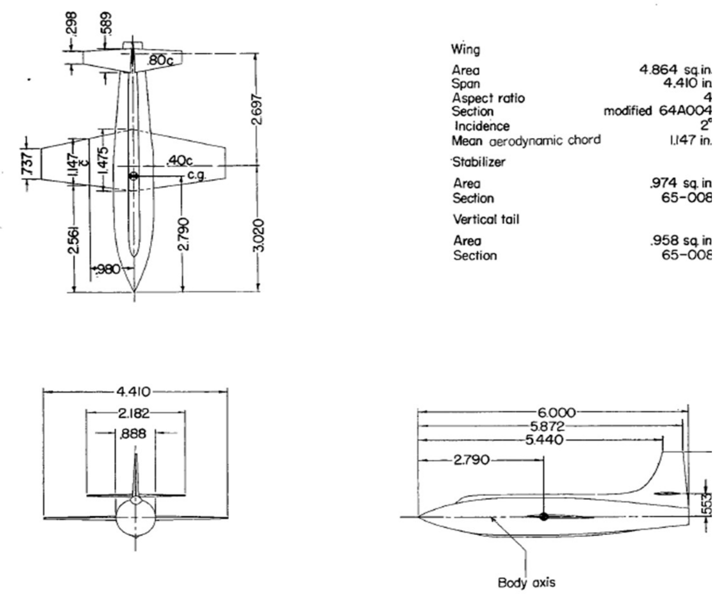

Wing	
Area	4.864 sq.in.
Span	4.410 in
Aspect ratio	4
Section	modified 64A004
Incidence	2°
Mean aerodynamic chord	1.147 in.
Stabilizer	
Area	.974 sq. in
Section	65-008
Vertical tail	
Area	.958 sq. in
Section	65-008

FIGURE 38 – Wind Tunnel Model Drawing of Bell X-1E from NASA TM-X-5. [29]

A. Bell X-1E

NASA TM-X-5 presents wind tunnel data results to determine the static stability characteristics of the Bell X-1E airplane. NASA found that the basic airplane became directionally unstable near Mach number 3; and that additional projected vertical fin area would help its directional stability. [29] At that time, NASA believed that their wind-tunnel test data was "reasonably indicative of flight data" collected by the USAF. [29] NASA presented X-1E longitudinal data in wind axis and its lateral-directional data was collected in body-axis; see FIGURE 38. Our *VORLAX* model is shown as FIGURE 39.

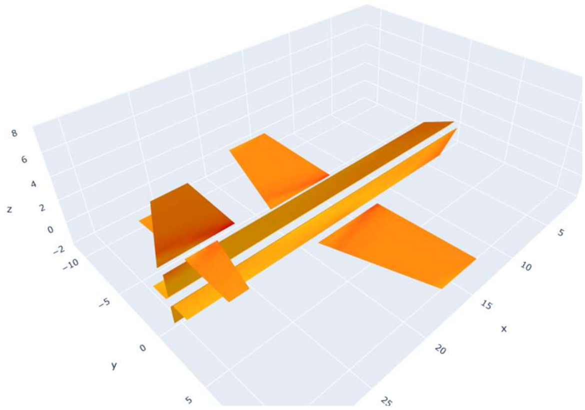

FIGURE 39 – *VORLAX2024* representation of the Bell X-1E

In FIGUREs 40 and 41, we compare *CL* vs *α*, *dCY/dβ*, *dCn/dβ* and *dCl/dβ* from the wind tunnel against *VORLAX*. *VORLAX2024d* captures the essential lateral/directional stability of this airframe. At both Mach 2.37 and Mach 4.01, we see an excellent correlation in lift, side force, directional stability, and dihedral effect with angle-of-attack. All test conditions represent flight with fully supersonic leading and trailing-edge flow conditions on the wing and tail.

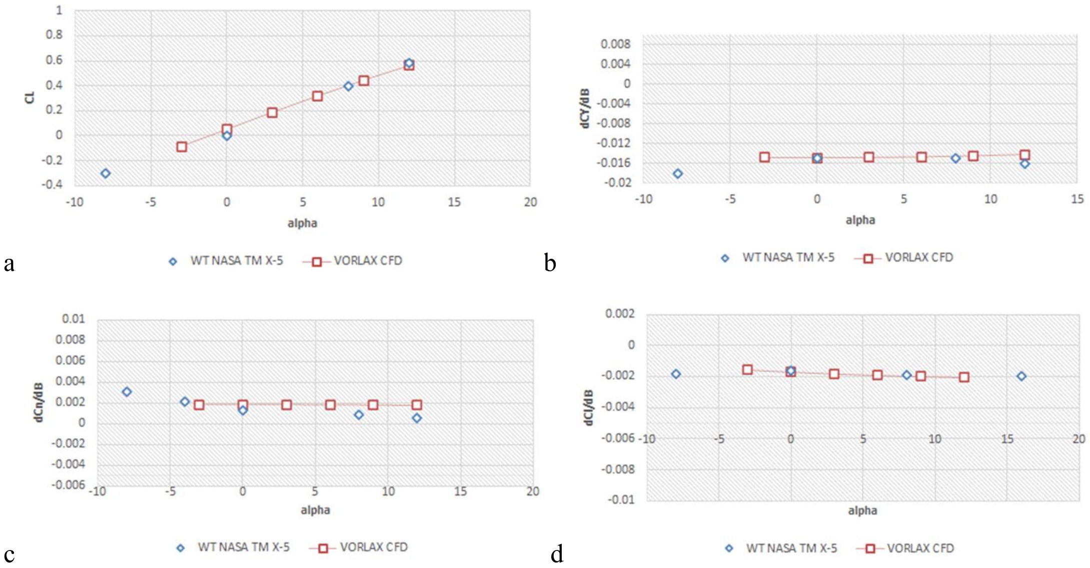

FIGURE 40 - Comparison between Wind Tunnel and *VORLAX2024d* for geometry from NASA TM-X-5 at M=2.37. a) *CL* vs *α*, b) *dCY/dβ* vs α, c) *dCn/dβ* vs α, d) *dCl/dβ* vs α. [29]

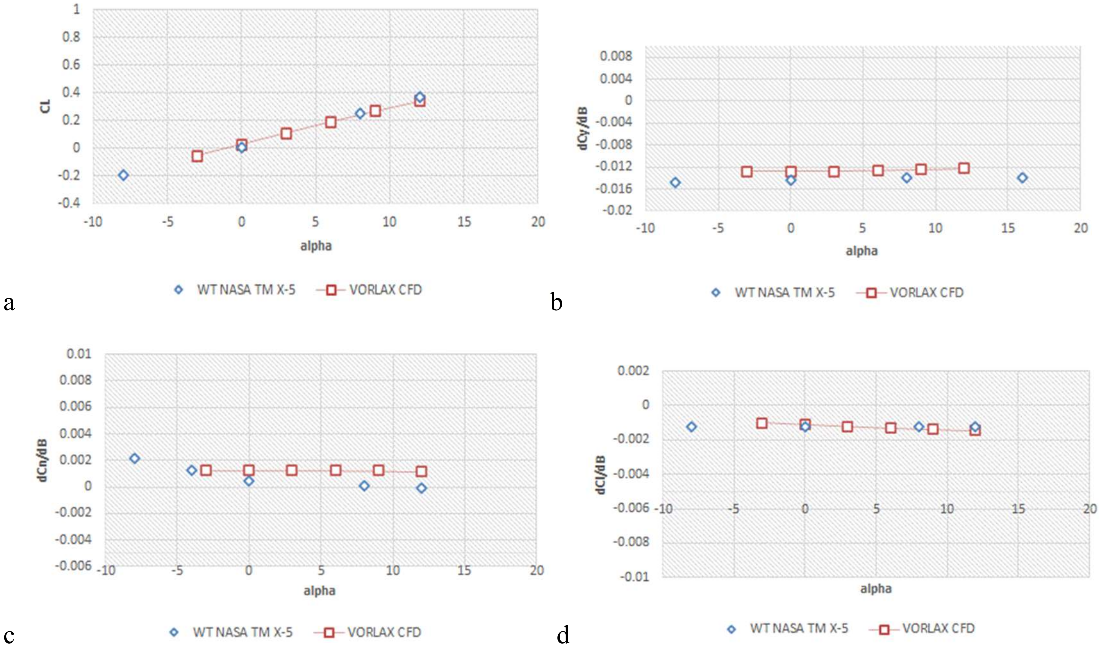

FIGURE 41 - Comparison between Wind Tunnel and *VORLAX2024d* for geometry from NASA TM-X-5 at M=4.01. a) *CL* vs *α*, b) *dCY/dβ* vs α, c) *dCn/dβ* vs α, d) *dCl/dβ* vs α. [29]

B. Bell X-2

Prior to flight test, limited Bell X-2 wind tunnel data was collected in the Langley 4- by 4-ft supersonic tunnel at Mach numbers of 1.40 and 1.59; see FIGURE 42. "A straight sting was used for pitch tests at zero yaw … while stings having 3° and 6° bends were used for pitch tests at … angle-of-attack." [30] This test indicated that the configuration's body-axis directional stability decreased with increasing Mach number while its effective body-axis dihedral is essentially invariant with both *CL* and Mach. Despite the presence of wing sweep, these test conditions represent flight with fully supersonic leading and trailing-edge flow conditions on the wing and tail.

In FIGURE 43, we compare the Mach 1.59 data for *CL* vs α, $dCY/d\beta$, $dCn/d\beta$ and $dCl/d\beta$ from wind tunnel against *VORLAX*. Once again, we see good to excellent correlation in lift, side force and directional stability and a somewhat weaker correlation in dihedral effect as *VORLAX2024d* shows a rising trend with dihedral effect increasing along with angle-of-attack (common to swept wing aircraft) while the wind tunnel shows dihedral effect to be essentially invariant to angle-of-attack.

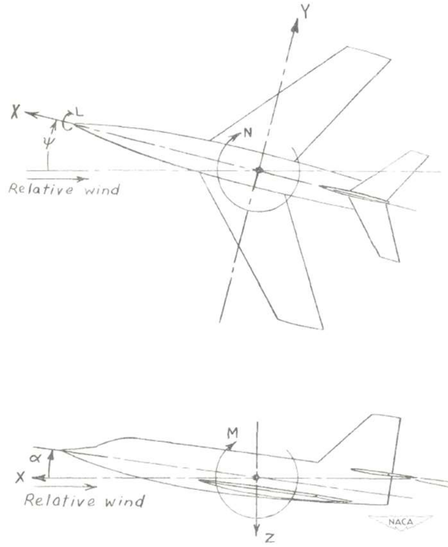

FIGURE 42 – Wind Tunnel Model Drawing of Bell X-2 from NACA RM L50C17. [30]

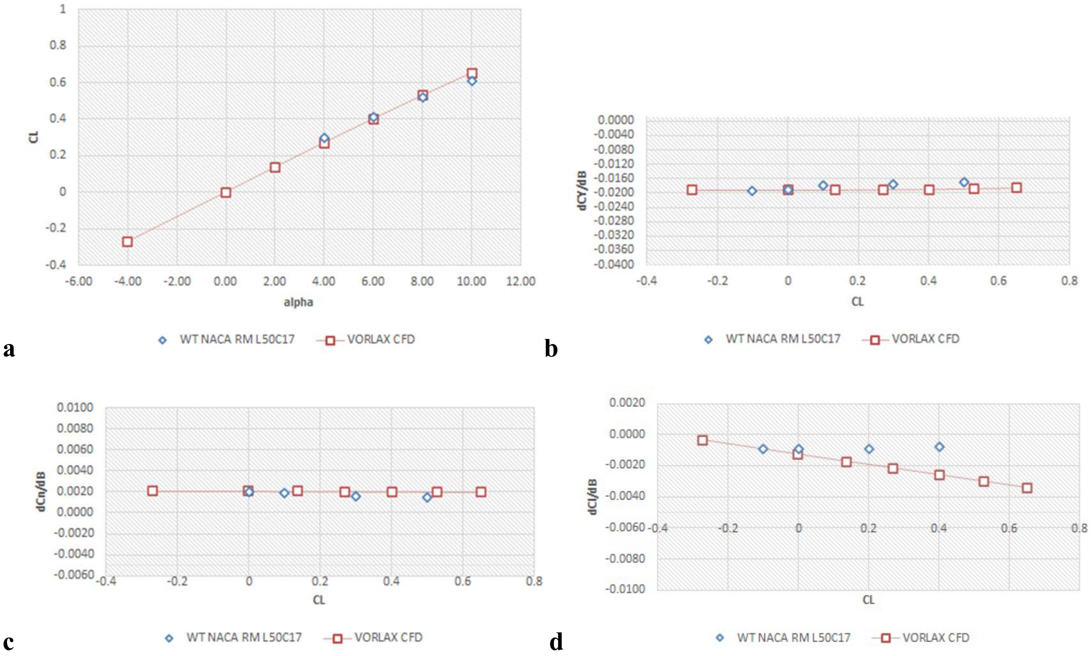

FIGURE 43 - Comparison between Wind Tunnel and *VORLAX2024d* for geometry from NACA RM L50C17 at M=1.59 a) *CL* vs α, b) $dCY/d\beta$ vs *CL*, c) $dCn/d\beta$ vs *CL*, d) $dCl/d\beta$ vs *CL*. [30]

C. Avro CF-105

NACA RM-SL58G28 presents an investigation in the Langley 4- by 4-ft supersonic pressure tunnel of the Canadian CF-105 aircraft at a variety of speeds; see FIGUREs 44 and 45. [31] Wind tunnel data is given with lift and drag in wind axis and the lateral/directional data in body axis.

In FIGUREs 46 and 47, we compare *CL* vs *α*, *dCY/dβ*, *dCn/dβ* and *dCl/dβ* from the wind tunnel and *VORLAX*. We see an excellent correlation in lift, and very good correlation in side force, directional stability, and dihedral effect at both test Mach numbers (1.6 and 2.0).

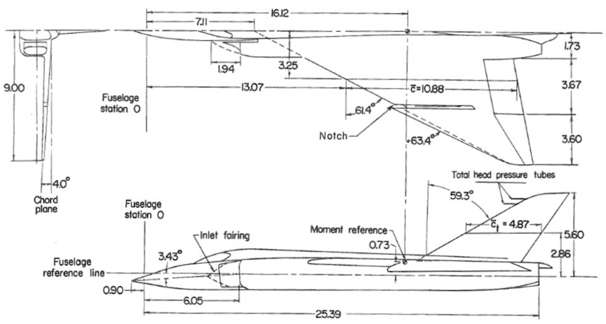

FIGURE 45 – Wind Tunnel Geometry from NACA RM-SL58G28. [31]

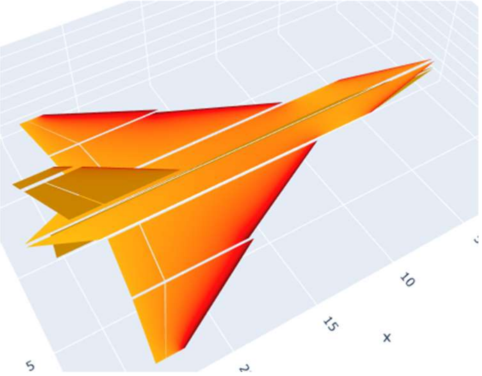

FIGURE 46 – *VORLAX2024* representation of the CF-105. [31]

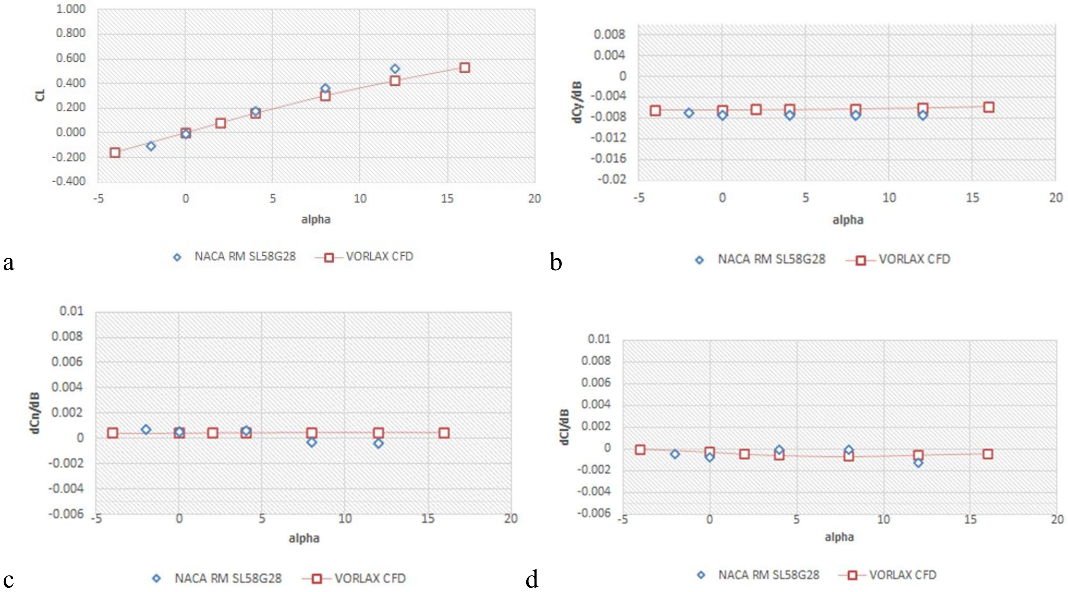

FIGURE 47 - Comparison between Wind Tunnel and *VORLAX* for geometry from NACA RM-SL58G28 at M=1.60 a) *CL* vs α, b) *dCY/dβ* vs α, c) *dCn/dβ* vs α, d) *dCl/dβ* vs α. [31]

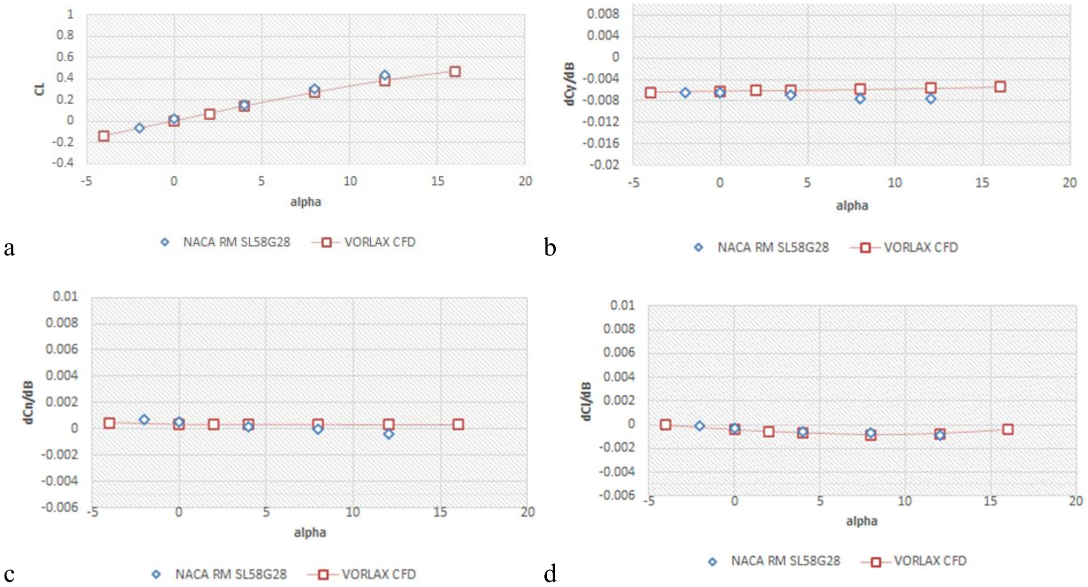

a b c d

FIGURE 48 - Comparison between Wind Tunnel and *VORLAX* for geometry from NACA RM-SL58G28 at M=2.00 a) *CL* vs α, b) *dCY/dβ* vs α, c) *dCn/dβ* vs α, d) *dCl/dβ* vs α. [31]

D. Lockheed F-104 Prototype

NACA RM-L56H06 presents an investigation in the Langley 4- by 4-ft supersonic pressure tunnel of a low-aspect-ratio unswept-wing airplane reminiscent of the production Lockheed F-104; see FIGUREs 49 and 50. [32] Wind tunnel data is given with lift and drag in wind axis and the lateral/directional data in body axis. With relatively unswept aerodynamic surfaces, this configuration represents a design where both the wing and the horizontal tail operate with supersonic leading edges at the test condition.

In FIGUREs 51 and 52, we compare *CL* vs *α*, *dCY/dβ*, *dCn/dβ* and *dCl/dβ* from the wind tunnel and *VORLAX*. We see an excellent correlation in lift, side force, directional stability, and dihedral effect at Mach 1.82.

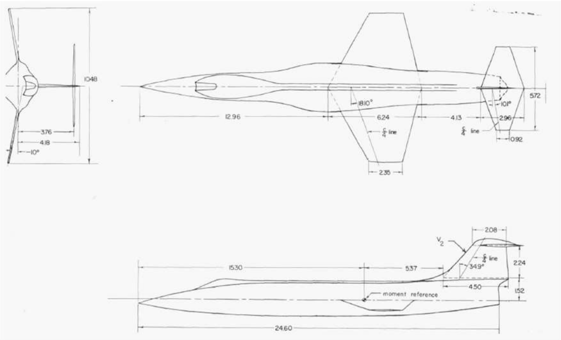

FIGURE 49 - Wind Tunnel Model Geometry from NACA RM L56-H06. [32]

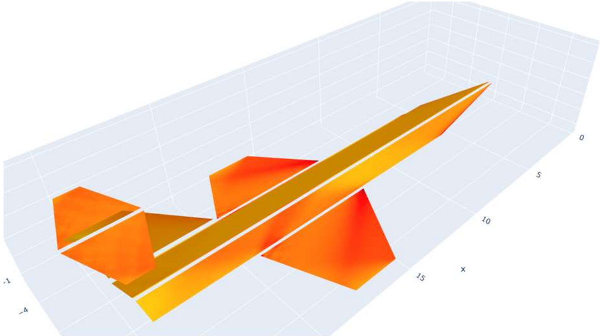

FIGURE 50 – *VORLAX2024* representation of the geometry in NACA RM L56-H06. [32]

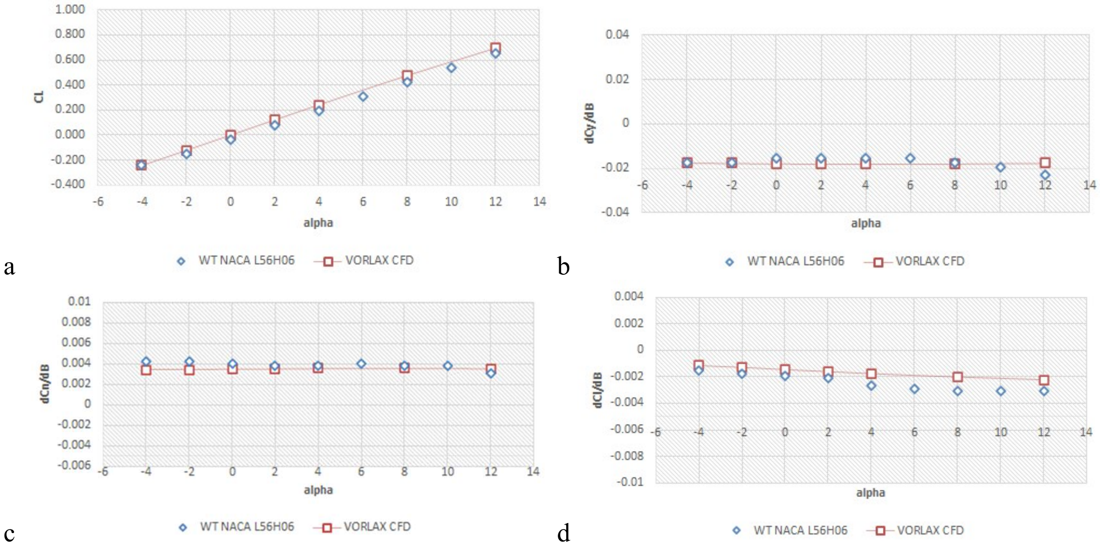

FIGURE 52 - Comparison between Wind Tunnel and *VORLAX* for geometry from NACA RM L56-H06 at M=1.81. a) *CL* vs α, b) *dCY/dβ* vs α, c) *dCn/dβ* vs α, d) *dCl/dβ* vs α. [32]

E. Lockheed Blackbird

Investigation of aerodynamic characteristics of a Lockheed Blackbird at the Langley Unitary Plan wind tunnel (4- by 4-ft); see FIGUREs 53 and 54. [33] To minimize cross-contamination of aerodynamic forces and moments by engine installation effects, Lockheed designed the model to have passive flow-through nacelles with constant internal cross sectional areas. Once again, the wind tunnel longitudinal data was presented in the wind axis while its lateral-directional data was collected in body-axis.

Force and moment data was collected from Mach 1.8 through 2.96. The Mach 1.8 data represents flight with a subsonic leading and supersonic trailing-edge flow conditions on the wing while the Mach 2.96 data represents flight with supersonic leading-edge and trailing-edge flow conditions on the wing.

In FIGUREs 55 and 56, we compare *CL* vs *α*, *dCY/dβ*, *dCn/dβ* and *dCl/dβ* from the wind tunnel and *VORLAX*. We see an excellent correlation in lift, and very good correlation in side force, directional stability, and dihedral effect at both test Mach numbers (1.8 and 2.96).

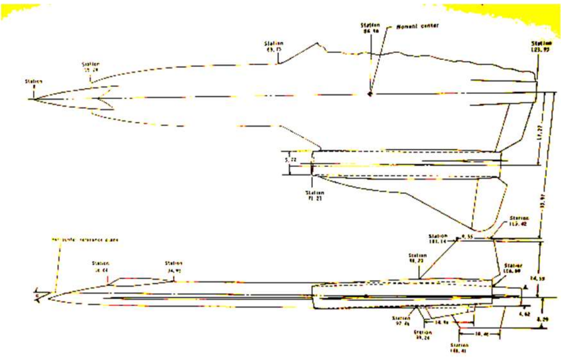

FIGURE 53 - Wind Tunnel Model Geometry from NASA TM-X-2524. [33]

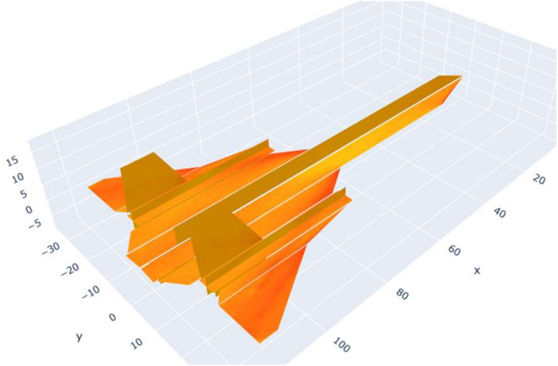

FIGURE 54 – *VORLAX2024* representation of the geometry in NASA TM-X-2524. [33]

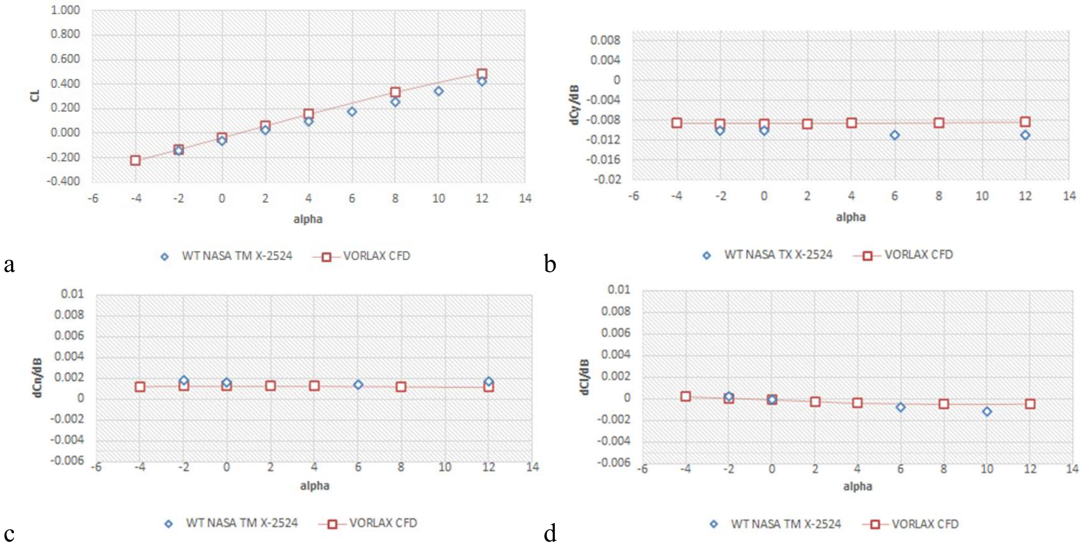

FIGURE 55 - Comparison between Wind Tunnel and *VORLAX* for geometry from NASA TM-X-2524 at M=1.80. a) *CL* vs α, b) *dCY/dβ* vs α, c) *dCn/dβ* vs α, d) *dCl/dβ* vs α. [33]

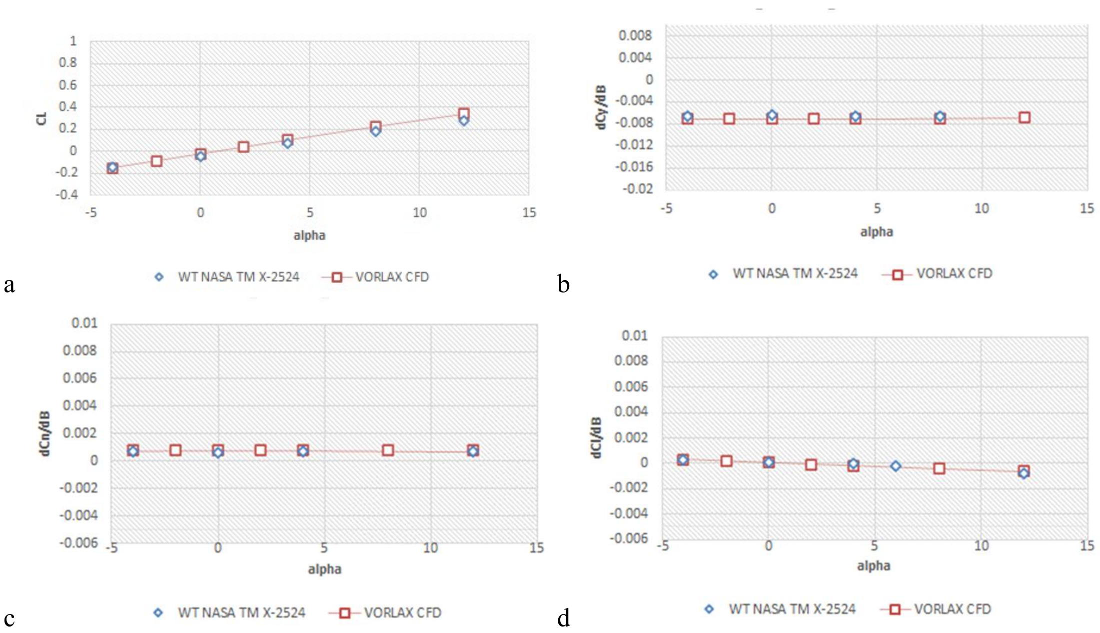

FIGURE 56 - Comparison between Wind Tunnel and *VORLAX* for geometry from NASA TM-X-2524 at M=2.96. a) *CL* vs α, b) *dCY/dβ* vs α, c) *dCn/dβ* vs α, d) *dCl/dβ* vs α. [33]

F. 60º Delta Wing Configuration

NASA TM-X-748 presents an investigation in the Langley 4- by 4-ft supersonic pressure tunnel of a 60º delta wing configuration; see FIGUREs 57 and 58. [34] Once again NASA presented the wind tunnel data with lift and drag in wind axis and the lateral/directional data in body axis. The test team noted that directional stability decreases as the angle-of-attack increases while directional stability increases as the vertical tail is made larger; the most effective vertical tail being one with a greater local aspect ratio (i.e., to make a larger, more effective tail, it should be taller).

This test was run at Mach 1.61; it presents flight with a subsonic leading and supersonic trailing-edge flow conditions on the wing.

In FIGURE 59, we compare *CL* vs α, $dCY/d\beta$, $dCn/d\beta$ and $dCl/d\beta$ from the wind tunnel and *VORLAX*. We see an excellent correlation in lift, side force, directional stability, and dihedral effect for this test case.

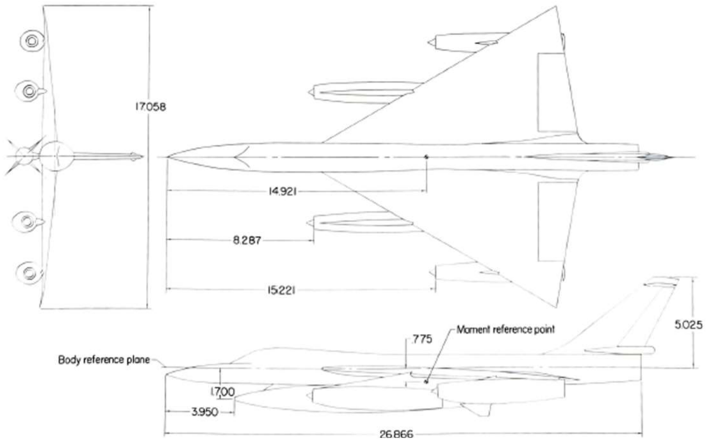

FIGURE 57 - Wind Tunnel Model Geometry from NASA TM-X-748. [34]

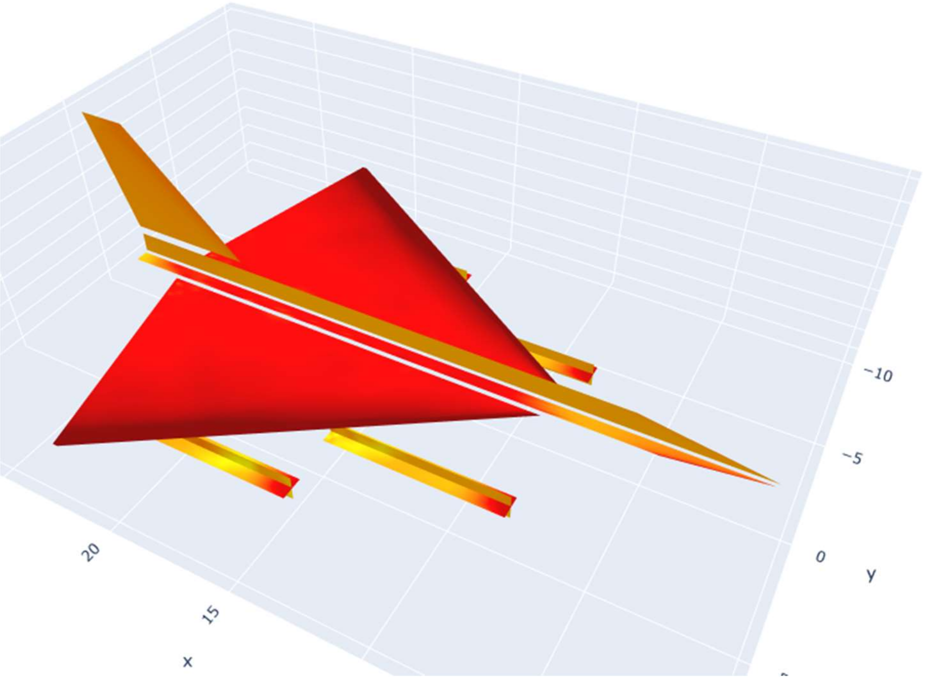

FIGURE 58 – *VORLAX2024* representation of the geometry from NASA TM-X-748. [34]

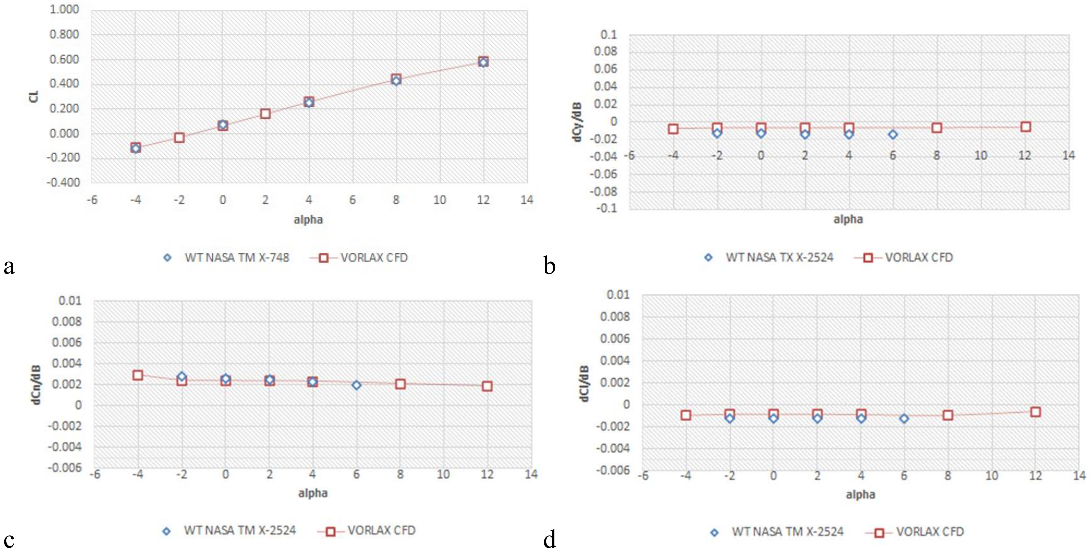

a b

c d

FIGURE 59 - Comparison between Wind Tunnel and *VORLAX* for geometry from NASA TM-X-537 at M=1.61 a) *CL* vs α, b) *Cm* vs *CL*, c) *dCY/dβ* vs α, d) *dCn/dβ* vs α, e) *dCl/dβ* vs α. [34]

G. Generic 1960's Variable Geometry Aircraft

NASA TM-X-1142 presents an investigation in the Langley 4- by 4-ft supersonic pressure tunnel of a variable geometry configuration at a variety of speeds; see FIGUREs 60 and 61. [35] NASA continues to present wind tunnel data with lift and drag in wind axis and the lateral/directional data in body axis.

For this comparison, we compare wind-tunnel to *VORLAX* for the 72.5^o leading edge sweep configuration tested at Mach 2.86. This represents flight with a subsonic leading and supersonic trailing-edge flow condition on the wing.

In FIGURE 62, we compare *CL* vs α, *dCY/dβ*, *dCn/dβ* and *dCl/dβ* from the wind tunnel and *VORLAX*. Once again, we see a very good correlation in lift, side force, directional stability, and dihedral effect at the test Mach number.

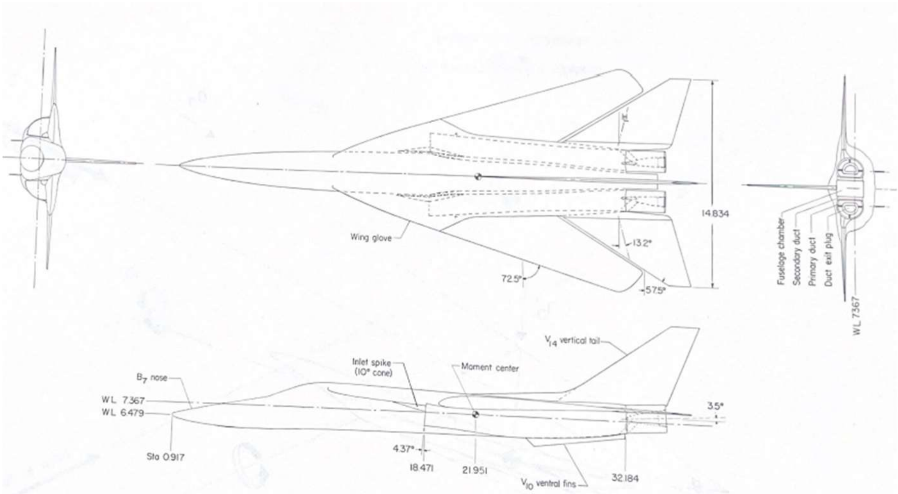

FIGURE 60 - Wind Tunnel Model Geometry from NASA TM-X-1142. [35]

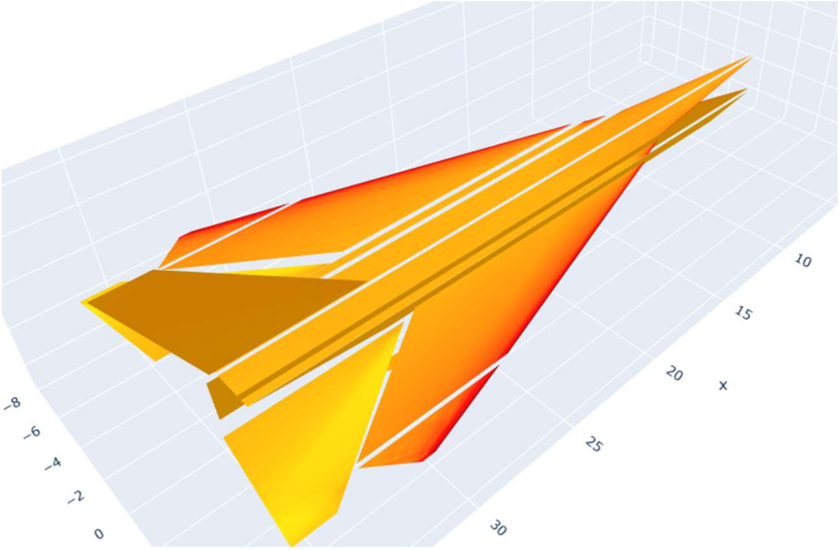

FIGURE 61 – *VORLAX* representation of the Geometry from NASA TM-X-1142. [35]

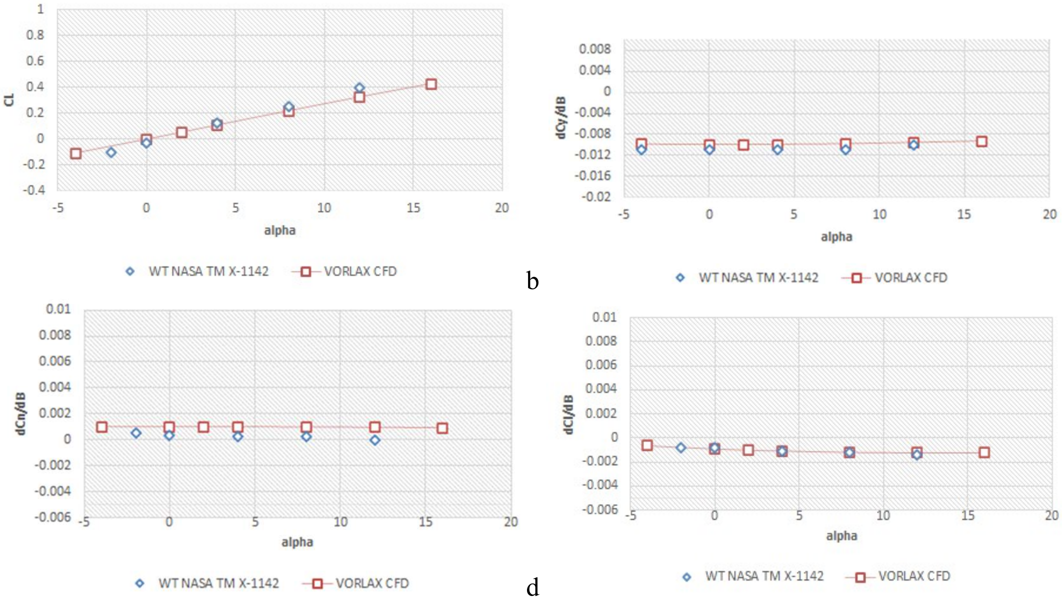

a b c d

FIGURE 62 - Comparison between Wind Tunnel and *VORLAX* for geometry from NASA TM-X-1142 at M=2.86.
a) *CL* vs α, b) *dCY/dβ* vs α, c) *dCn/dβ* vs α, d) *dCl/dβ* vs α. [35]

VII. Results & Conclusions

We continue to be amazed at the utility of Luis R. Miranda's *VORLAX* code.

Our 2024 upgrade package highlights refinements made to improve this code. Although limitations in the theory remain, careful use of *VORLAX* will allow for rapid processing of geometries at subsonic, transonic, and supersonic flight conditions. Our code changes comprise general usability upgrades which improve solution robustness, revisions to the manner by which *VORLAX* estimates and integrates pressure fields, and changes to improve the quality of lateral-directional moment prediction.

We made specific changes which:

- Improve solution robustness by limiting the "gain" of the Prandtl-Glauert / Ackeret transformation to avoid the sonic "singularity." The gain in lift due to freestream Mach number is thus limited to ~2 times the incompressible value.
- Improve solution robustness at supersonic speeds through an algorithm change when a "Mach Cone" line falls across an interior field panel. Instead of broadly suppressing node points (which makes the solution unnecessarily near-singular), the code now only suppresses node points when the grid field precisely aligns with an implied Mach cone angle.
- Has the code output "-999" for coefficients for a poorly converged solution; this makes it easier to error trap the solutions in post-processing.
- Revise pressure field estimations for both double-impermeable (conventional, "thin" panels) and single-impermeable ("sandwich panels") to account for maximum stagnation pressures, maximum pressures associated with attached turning flows and minimum pressures associated with a 70% vacuum.

VORLAX now:

- Integrates the resulting pressure fields first into the body axis. For output, the integrated forces and moments are transformed into USAF standard stability axis.
- Estimates significantly different rolling moments-due-to-sideslip, as the magnitude of the *SICPLE* correction has been reduced by a factor of three. This empirical choice of the appropriate "gain" for *SICPLE* has been selected to best match *VORLAX* estimations of rolling-moment-due-to-sideslip to wind tunnel test data.

The paper includes validation cases for pressure fields over basic wing forms (NACA 4-digit, biconvex and wedge) at subsonic and supersonic speeds.

The paper includes validation cases for forces and moments for a variety of aircraft from subsonic (the Boeing 707) through hypersonic (the North American X-15) speeds. Especial consideration has been made to show the accuracy of predicted lateral-directional stability across a wide variety of high-speed aircraft, both swept (ex. Avro CF-105 and Convair B-58) and unswept (ex. Bell X-1 and Lockheed F-104).

Acknowledgements

This revised version of *VORLAX* (*VORLAX2024d*) has been released and is available at: https://labs.engineering.asu.edu/aircraft-design/

This manuscript derives from the work Mr. Gaydusek and Mr. Lorenzo performed in partial fulfillment of the degree requirements to obtain their M.S. degrees in Aerospace Engineering from Arizona State University.

Professor Takahashi's research was supported in part by an appointment to the Department of Defense (DOD) Research Participation Program administered by the Oak Ridge Institute for Science and Education (ORISE) through an interagency agreement between the U.S. Department of Energy (DOE) and the DOD. ORISE is managed by ORAU under DOE contract number DE-SC0014664. All opinions expressed in this paper are the authors' and do not necessarily reflect the policies and views of DOD, DOE, or ORAU/ORISE.

Professor Takahashi would like to thank his AFIT collaborators Prof. Ramana V. Grandhi and Prof. José Camberos for inspiration and encouragement to undertake continued development of *VORLAX*.

Professor Takahashi would also like to thank his longtime friend and colleague Dr. Patrick Rodi for discussions on *Cp*max.

Special thanks to Kevin O'Brien for developing the initial Bell X-2 *VORLAX* model.

References

[1] Joshi, H. and Thomas, P., "Review of Vortex Lattice Method for Supersonic Aircraft Design," The Aeronautical Journal , Volume 127 , Issue 1317 , November 2023 , pp. 1869 – 1903.

[2] Miranda, L. R., Elliot, R. D., and Baker, W. M., "A Generalized Vortex Lattice Method for Subsonic and Supersonic Flow Applications." NASA CR 2865, 1977.

[3] Souders, T. J., & Takahashi, T. T., "VORLAX 2020: Benchmarking Examples of a Modernized Potential Flow Solver." AIAA 2021-2459, 2021.

[4] Souders, T. J., & Takahashi, T. T., "VORLAX 2020: Making a Potential Flow Solver Great Again." AIAA 2021-2458, 2021.

[5] Souders, T.J., Heimtann, K.M. and Takahashi, T.T., " Life in the Fast Lane: Project-Based Learning of Advanced Aerodynamics Using a Rapid Potential Flow Code," AIAA 2022-1350,2022.

[6] Drela, M. and Youngren, H., "AVL (3.30) User Primer, AVL Overview," 2010. See: http://web.mit.edu/drela/Public/web/avl/avl_doc.txt (retrieved May 2024).

[7] *See:* https://tornado.redhammer.se/images/manual.pdf (retrieved May 2024).

[8] *See:* https://openvsp.org/wiki/doku.php?id=vspaerotutorial (retrieved May 2024).

[9] Ward, G.N., Linearized Theory of Steady High-Speed Flow. Cambridge University Press, 1955.

[10] Alexander, M., "USAF Wind Tunnel Handbook," WL-TR-91-3073

[11] Walker, H.J., and Wolowicz, C.H., "Theoretical Stability Derivatives for the X-15 Research Airplane at Supersonic and Hypersonic Speeds Including a Comparison with Wind-tunnel Results," NASA TM-X-287, 1960.

[12] Smith, A.M.O. "High Lift Aerodynamics" AIAA J. Aircraft, Vol. 12, No. 6, 1975.

[13] Anon., "Equations, Tables and Charts for Compressible Flow," NACA 1135, 1953.

[14] *See:* https://archive.aoe.vt.edu/mason/Mason_f/ConfigAeroHypersonics.pdf (retrieved May 2024).

[15] Anderson, J.D., Hypersonic and High-Temperature Gas Dynamics, 3rd Edition, AIAA, 2019.

[16] Abbott, I.H., von Doenhoff, A.E. and Stivers, L., "Summary of Airfoil Data," NACA TR-824, 1945.

[17] Alexander, S.R., "Drag Measurements of Symmetrical Circular-Arcand Nica 65-009 Rectangular Airfoils Having an Aspect Ratio of 2.7 as Determined by Flight Tests at Supersonic Speeds" NACA RM L6J14, 1947.

[18] McLellan, C.H., "A Method for Increasing the Effectiveness of Stabilizing Surfaces at High Supersonic Mach Numbers," NACA RM L54F21, 1954.

[19] Brooks, E.N., Jr., Decker, J.P. and Blackwell, J.A., Jr., "Static Aerodynamic Characteristics of a Model of a Typical Subsonic Jet-Transport Airplane at Mach Numbers from 0.40 to 1.20," NASA TM X-1345, 1967.

[20] Kuhn, R.E. & Wiggins, J.W., "Static Lateral Stability Characteristics of a 1/10th Scale Model of the X-1 Airplane at High Subsonic Speeds," NACA RM L51F01a, 1951.

[21] Henderson, A., "Wind Tunnel Investigation of the Static Longitudinal and Lateral Stability of the Bell X-1A at Supersonic Speeds," NACA RM L55I12, 1955.

[22] Gera, J., "Exploratory Tests for Airplane Stability and Control Effectiveness in a Low-Density Wind Tunnel at Mach Numbers of 3, 4.5 and 6." NASA TM-X-1308, 1966.

[23] Martin, G.L., "Paneling Techniques for use with the VORLAX Computer Program." NASA-CR-145364. 1978.

[24] Mattson, A.T., "Force and Longitudinal Control Characteristics of a 1/16 Scale Model of the Bell XS-1 Transonic Research Airplane at High Mach Numbers," NACA RM L7A03, 1947.

[25] Drake, H.M., and Stillwell, W.H., "Behavior of the Bell X-1A Research Airplane During Exploratory Flights at Mach Numbers near 2.0 and at Extreme Altitudes," NACA RM H55G25, 1955.

[26] Lorenzo, W.P. and Takahashi, T.T., "A Reassessment of the Controllable Flight Envelope of the Bell X-1A Rocket Plane," AIAA 2024-4138, 2024.

[27] Uribe-Quintero, E., and Takahashi, T.T., "Flight Dynamics Issues of Control Coupling / Inertia Coupling Prone High-Speed Aircraft," AIAA 2024-4048, 2024.

[28] Henderson, A., Jr., "Wind-Tunnel Investigation of Static Lateral and Longitudinal Stability Characteristics of the 1/62-Scale Model of the X-1E Airplane at Combined Angles of Attack and Sideslip at Supersonic Speeds," NACA RM L57G22, 1957.

[29] Smith, F.M., "Wind Tunnel Investigation of the Static Stability of a 1/56-Scale Model of the X-1E Airplane at Mach Numbers of 2.37, 2.98 and 4.01," NASA TM X-5, 1959.

[30] Spearman, M.L., "An Investigation of a Supersonic Aircraft Configuration Having a Tapered Wing with Circular-Arc Sections and 40° Sweepback – Static Lateral-Stability Characteristics at Mach 1.40 and 1.59," NACA RM L50C17, 1950.

[31] Silvers, H.N., Fournier, R.H., Wills, J.S., "Longitudinal and Lateral Stability and Control Characteristics and Vertical Tail Load Measurements for a 0.03-Scale Model of the Avro CF-105 Airplane at Mach Numbers of 1.60, 1.80 and 2.00," NACA RM SL58G28, 1958.

[32] Spearman, M.L. and Driver, C., "Longitudinal and Lateral Stability Characteristics of a Low-Aspect-Ratio Unswept-Wing Airplane Model at Mach Numbers of 1.82 and 2.01," NACA RM L56H06, 1957.

[33] Lamb, M., Stallings, R.L., Jr. and Richardson, C.S., "Aerodynamic Characteristics of 1/25-scale model of YF-12 Airplane at Mach 1.80 to 2.96 with and without external instrument packages and Flow-Field Surveys at Mach 2.96," NASA TM-X-2524, 1972.

[34] Landrum, E.J., "Static Lateral and Directional Stability and Control Characteristics of a 1/40-scale Model of a 60° Delta Wing Bomber Configuration at a Mach Number of 1.61," NASA TM-X 748, 1963.

[35] Shaw, D.S., and Campbell, J.F., "Supersonic Investigation of the Static Stability, Performance and Control of a Variable Sweep Tactical Fighter Model – Phase 3," NASA TM X-1142, 1965.